Calculation of predictions for non-identical particle correlations in heavy ions collisions at LHC energies from hydrodynamics-inspired models

MASTER OF SCIENCE THESIS

Author:
Mateusz Wojciech Gałażyn

Supervisor:
Prof. Adam Kisiel

Warsaw, 20th November 2014

Wyznaczenie przewidywań teoretycznych dla korelacji cząstek nieidentycznych w zderzeniach ciężkich jonów przy energiach LHC w modelach opartych na hydrodynamice

PRACA MAGISTERSKA

Autor:
Mateusz Wojciech Gałażyn

Promotor:
dr hab. inż. Adam Kisiel, prof. PW

Warszawa, 20 listopada 2014

Abstract

This thesis presents results of two-particle momentum correlations analysis for different kinds of particles produced in heavy ion collisions. The studies were carried for the data from lead-lead collisions at the centre of mass energy $\sqrt{s_{NN}} = 2.76$ TeV simulated in the THERMINATOR model using the (3+1)-dimensional hydrodynamic model with viscosity. Analysis was performed for the three particle kinds: pions, kaons and protons for the collisions in eight different centrality ranges.

The THERMINATOR model allows to perform statistical hadronization of stable particles and unstable resonances from a given hypersurface which is followed by the resonance propagation and decay phase. The four-dimensional hypersurface is coming from the calculations performed on a basis of relativistic hydrodynamic framework with the viscosity corrections.

One can investigate space-time characteristics of the particle-emitting source through two-particle interferometry using experimental observables. The experimental-like analysis of the data coming from a model calculations yields a possibility to test the hydrodynamic description of a quark-gluon plasma. This thesis concentrates on the verification of the prediction of appearance of femtoscopic radii scaling with the transverse mass.

The three dimensional correlation functions were calculated using spherical harmonics decomposition. One can use this approach to perform calculations with lower statistics and the visualization of results is much easier. The calculated correlation functions show expected increase of a correlation for pions and kaons at the low relative momenta of a pair. For the protons at the same momentum region, the decrease occurs. The transverse pair momentum and centrality dependence on a correlation function is observed. In order to perform the quantitative analysis of this influence, the fitting of theoretical formula for correlation function was performed. The femtoscopic radii calculated in the LCMS and PRF are falling with the transverse mass m_T. To test the scaling predicted from the hydrodynamics, the power law was fitted $\alpha m_T^{-\beta}$. The radii calculated for pions, kaons and protons in the LCMS are following the common scaling. In case of the PRF no such scaling is observed. To recover the scaling in the PRF, the approximate factor is proposed: $\sqrt{\left(\sqrt{\gamma_T}+2\right)/3}$. The radii in the PRF divided by the proposed scaling factor are falling on the common curve, therefore the scaling can be recovered using the proposed scaling factor. The experimental analysis is usually performed in the PRF (requires less statistics), hence the method of scaling recovery enables easier testing of the hydrodynamic predictions, which are not visible in the PRF.

Streszczenie

W tej pracy zaprezentowane są wyniki analizy dwucząstkowych korelacji pędowych dla trzech różnych typów cząstek produkowanych w zderzeniach ciężkich jonów. Obliczenia zostały wykonane dla danych ze zderzeń ołów-ołów przy energii w centrum masy $\sqrt{s_{NN}} = 2.76$ TeV wygenerowanych za pomocą modelu `THERMINATOR` przy użyciu (3+1)-wymiarowego modelu hydrodynamicznego uwzględniającego lepkość ośrodka. Analiza została wykonana dla trzech rodzajów cząstek: pionów, kaonów i protonów dla dziewięciu różnych przedziałów centralności.

Model `THERMINATOR` pozwala na wykonanie statystycznej hadronizacji stabilnych cząstek jak i również niestabilnych rezonansów z danej hiperpowierzchni wymrażania oraz uwzględnienie propagacji i rozpadów tych rezonansów. Czterowymiarowa hiperpowierzchnia pochodzi z obliczeń przeprowadzonych na podstawie hydrodynamiki relatywistycznej z uwzględnieniem poprawek pochodzących od lepkości.

Interferometria dwucząstkowa pozwala na zbadanie charakterystyk czasowo-przestrzennych źródła cząstek. Poprzez analizę danych pochodzących z obliczeń modelowych można dokonać sprawdzenia zakresu stosowalności hydrodynamiki do opisu właściwości plazmy kwarkowo-gluonowej. Ta praca koncentruje się na weryfikacji skalowania promieni femtoskopowych z masą poprzeczną przewidywanego przez hydrodynamikę.

Trójwymiarowe funkcje korelacyjne zostały obliczone za pomocą rozkładu w szereg harmonik sferycznych. To podejście wymaga mniejszej statystyki i pozwala na łatwiejszą wizualizację wyników. Obliczone funkcje korelacyjne wykazują oczekiwany wzrost korelacji dla niskich różnic pędów dla par pionów i kaonów. Dla par protonów w tym samym zakresie pędów widoczny jest spadek korelacji. Widoczny jest wpływ pędu poprzecznego pary oraz centralności na funkcję korelacyjną. W celu wykonania analizy ilościowej tego wpływu, zostało wykonane dopasowanie formuły analitycznej do obliczonych funkcji korelacyjnych. Otrzymane w ten sposób promienie femtoskopowe w LCMS i PRF wykazują spadek wraz z wzrostem masy poprzecznej m_T. W celu sprawdzenie skalowania przewidywanego przez hydrodynamikę została dopasowana zależność potęgowa: $\alpha m_T^{-\beta}$. Promienie obliczone dla pionów, kaonów i protonów zachowują wzajemne skalowanie w LCMS. W przypadku PRF skalowanie nie jest widoczne. Aby odzyskać skalowanie w PRF, został zaproponowany przybliżony współczynnik: $\sqrt{\left(\sqrt{\gamma_T}+2\right)/3}$. Promienie w PRF po podzieleniu przez

współczynnik skalowania, są opisywalne przez podaną zależność potęgową, zatem umożliwia on odzyskanie skalowania. Analiza eksperymentalna jest zazwyczaj wykonywana w PRF (wymaga mniejszej statystyki), zatem ta metoda pozwala na łatwiejszą weryfikację przewidywań hydrodynamiki które są widoczne w LCMS, a nie są w PRF.

Contents

Introduction

Many people were trying to discover what was in the beginning of the universe which we observe today. Through the years, more or less successful theories were appearing and trying to describe its origin and behaviour. Among them is one model, which provides a comprehensive explanation for a broad range of phenomena, including the cosmic microwave background, abundance of the light elements and Hubble's law. This model is called The Big Bang theory and has born in 1927 on the basis of principles proposed by the Belgian priest and scientist Georges Lemaître. Using this model and known laws of physics one can calculate the characteristics of the universe in detail back in time to the extreme densities and temperatures. However, at some point these calculations fail. The extrapolation of the expansion of universe backwards in time using general relativity yields an infinite density and temperature at a finite time in the past. This appearance of singularity is a signal of the breakdown of general relativity. The range of this extrapolation towards singularity is debated - certainly we can go no closer than the end of *Planck epoch* i.e. 10^{-43} s. At this very first era the temperature of the universe was so high, that the four fundamental forces - electromagnetism, gravitation, weak nuclear interaction and strong nuclear interaction - were one fundamental force. Between 10^{-43} s and 10^{-36} s of a lifetime of the universe, there is a *grand unification epoch*, at which forces are starting to separate from each other. The *electroweak epoch* lasted from 10^{-36} s to 10^{-12} s, when the strong force separated from the electroweak force. After the electroweak epoch, there was the *quark epoch* in which the universe was a dense "soup" of quarks. During this stage the fundamental forces of gravitation, electromagnetism, strong and weak interactions had taken their present forms. The temperature at this moment was still too high to allow quarks to bind together and form hadrons. At the end of quark era, there was a big freeze-out - when the average energy of particle interactions had fallen below the binding energy of hadrons. This era in which quarks became confined into hadrons is known as the hadron epoch. At this moment the matter had started forming nuclei and atoms, which we observe today.

Here arises the question: how can we study the very beginning of the universe? To do this, one should create in a laboratory a system with such a large density and high temperature to recreate those conditions. Today, this is achievable through sophisticated machines, which are particle accelerators. In the particle accelerators, like the Large Hadron Collider at CERN, Geneva or

Relativistic Heavy Ion Collider at Brookhaven National Laboratory in Upton, New York, the heavy ions after being accelerated to near the speed of light are collided in order to generate extremely dense and hot phase of matter and recreate the quark-gluon plasma. The plasma is believed to behave like an almost ideal fluid and to become a medium, that can be described by the laws of relativistic hydrodynamics.

This thesis is providing predictions for collective behaviour of the quark-gluon plasma coming from the hydrodynamic equations. Experimental-like analysis was performed for the high energy Pb-Pb collisions generated with `THERMINATOR` model.

The 1st chapter is an introduction to the theory of heavy ion collisions. It contains the brief description of the Standard Model and Quantum Chromodynamics. The quark-gluon plasma and its signatures are also characterized.

In the 2nd chapter there is a description of the relativistic hydrodynamic framework and the `THERMINATOR` model used to perform the simulations of collisions.

The 3rd chapter covers the particle interferometry method used in this work. The algorithm of building experimental correlation functions and effects coming from the hydrodynamics in the experimental results for particle interferometry are also presented.

In the 4th chapter there is a detailed analysis of the results for two-particle femtoscopy for different pairs of particles. The quantitative analysis of calculated femtoscopic radii as well as the appearance of transverse mass scaling is discussed.

Chapter 1

Theory of heavy ion collisions

1.1 The Standard Model

In the 1970s, a new theory of fundamental particles and their interaction emerged. It was a new concept, which combines the electromagnetic, weak and strong nuclear interactions between know particles. This theory is called *The Standard Model*. There are seventeen named particles in the standard model, organized into the chart shown below (Fig. 1.1). Fundamental particles are divided into two families: *fermions* and *bosons*.

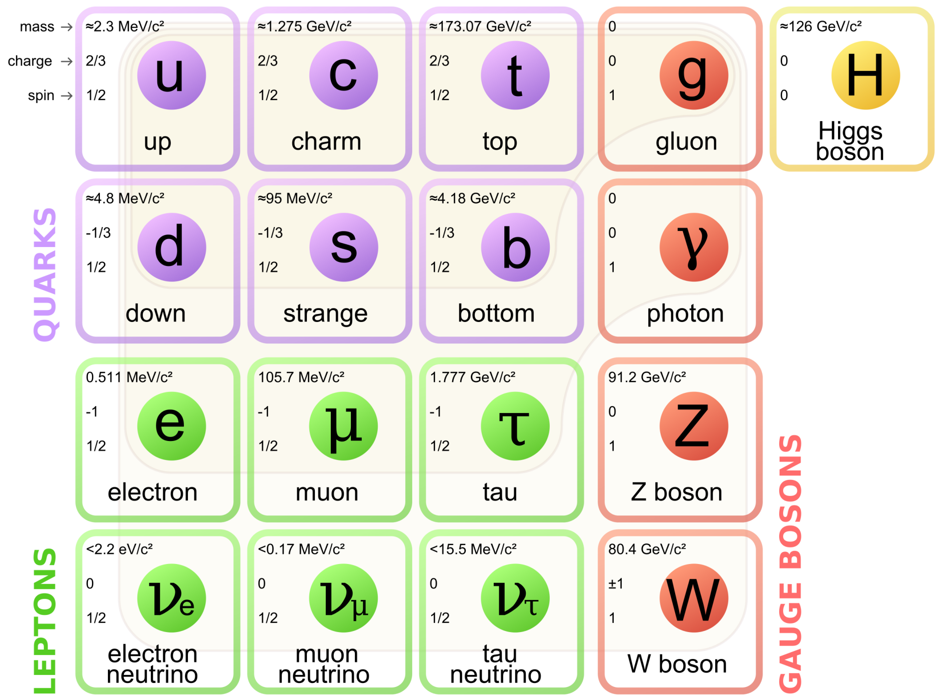

Figure 1.1: The Standard Model of elementary particles [1].

Fermions are the building blocks of matter. They are divided into two groups. Six of them, which must bind together are called *quarks*. Quarks are known to bind into doublets (*mesons*), triplets (*baryons*) and recently confirmed four-quark states.[1] Two of baryons, with the longest lifetimes, are forming a nucleus: a proton and a neutron. A proton is build from two up quarks and one down, and neutron consists of two down quarks and one up. A proton is found to be a stable particle (at least it has a lifetime larger than 10^{35} years) and a free neutron has a mean lifetime about 8.8×10^2 s. Fermions, that can exist independently are called *leptons*. Neutrinos are a subgroup of leptons, which are only influenced by weak interaction. Fermions can be divided into three generations (three columns in the Figure 1.1). Generation I particles can combine into hadrons with the longest life spans. Generation II and III consists of unstable particles which also form unstable hadrons.

Bosons are force carriers. There are four fundamental forces: weak - responsible for radioactive decay, strong - coupling quarks into hadrons, electromagnetic - between charged particles and gravity - the weakest, which causes the attraction between particles with mass. The Standard Model describes the first three. The weak force is mediated by $W^{\pm}$ and Z^0 bosons, electromagnetic force is carried by photons γ and the carriers of a strong interaction are gluons *g*. The fifth boson is a Higgs boson which is responsible for giving other particles mass.

1.2 Quantum Chromodynamics

1.2.1 Quarks and gluons

Quarks interact with each other through the strong interaction. The mediator of this force is a *gluon* - a massless and electrical chargeless particle. In the quantum chromodynamics (QCD) - theory describing strong interaction - there are six types of "charges" (like electrical charges in the electrodynamics) called *colours*. The colours were introduced because some of the observed particles, like Δ^-, Δ^{++} and Ω^- appeared to consist of three quarks with the same flavour (*ddd*, *uuu* and *sss* respectively), which was in conflict with the Pauli principle. One quark can carry one of the three colours (usually called *red*, *green* and *blue*) and antiquark one of the three anti-colours respectively. Only colour-neutral (or white) particles could exist. Mesons are assumed to be a colour-anticolour pair, while baryons are *red-green-blue* triplets. Gluons also are colour-charged and there are 8 types of gluons. Therefore they can interact with themselves [3].

[1] The LHCb experiment at CERN in Geneva confirmed recently the existence of $Z(4430)$ - a particle consisting of four quarks [2].

1.2.2 Quantum Chromodynamics potential

As a result of the fact that gluons are massless, one can expect, that the static potential in QCD will have the form like similar one in electrodynamics e.g. $\sim 1/r$ (through analogy to photons). In reality the QCD potential is assumed to have the form of [3]

$$V_s = -\frac{4}{3}\frac{\alpha_s}{r} + kr \ , \tag{1.1}$$

where the α_s is a coupling constant of the strong force and the kr part is related with *confinement*. In comparison to the electromagnetic force, a value of the strong coupling constant is $\alpha_s \approx 1$ and the electromagnetic one is $\alpha = 1/137$.

The fact that quarks does not exist separately and are always bound, is called confinement. As two quarks are pulled apart, the linear part kr in the Eq. 1.1 becomes dominant and the potential becomes proportional to the distance. This situation resembles stretching of a string. At some point, when the string is so large it is energetically favourable to create a quark-antiquark pair. At this moment such pair (or pairs) is formed, the string breaks and the confinement is preserved (Fig. 1.2).

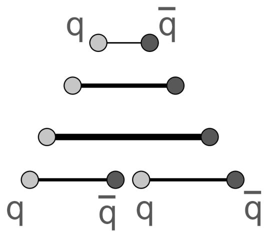

Figure 1.2: A string breaking and a creation of a new quark-anti-quark pair [4].

On the other hand, for small r, an interaction between the quarks and gluons is dominated by the Coulomb-like term $-\frac{4}{3}\frac{\alpha_s}{r}$. The coupling constant α_s depends on the four-momentum Q^2 transferred in the interaction. This dependence is presented in Fig. 1.3. The value α_s decreases with increasing momentum transfer and the interaction becomes weak for large Q^2, i.e. $\alpha_s(Q) \rightarrow 0$. Because of the weakening of coupling constant, quarks at large energies (or small distances) are starting to behave like free particles. This phenomenon is known as *asymptotic freedom*. The QCD potential also has temperature dependence - the force strength "melts" with the temperature increase. Therefore the asymptotic freedom is expected to appear in either the case of high baryon densities (small distances between quarks) or very high temperatures. This temperature dependence is illustrated in Fig. 1.4.

If the coupling constant α_s is small, one can use perturbative methods to calculate physical observables. Perturbative QCD (pQCD) successfully describes hard processes (with large Q^2), such as jet production in high energy proton-antiproton collisions. The applicability of pQCD is defined by the *scale parameter*

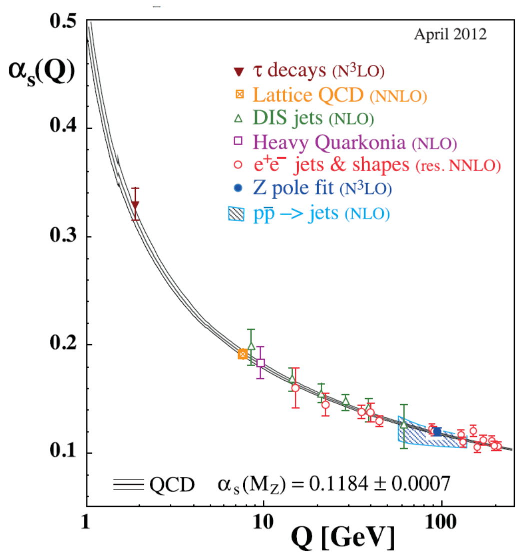

Figure 1.3: The coupling parameter α_s dependence on four-momentum transfer Q^2 [5].

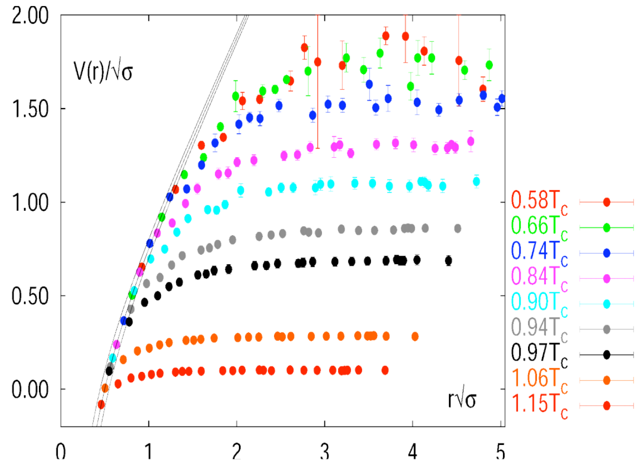

Figure 1.4: The QCD potential for a quark-antiquark pair as a function of distance for different temperatures. A value of a potential decreases with the temperature [4].

$\Lambda_{QCD} \approx 200$ MeV. If $Q \gg \Lambda_{QCD}$ then the process is in the perturbative domain and can be described by pQCD. A description of soft processes (when $Q < 1$ GeV) is a problem in QCD - perturbative theory breaks down at this scale. Therefore, to describe processes with low Q^2, one has to use alternative methods like Lattice QCD. Lattice QCD (LQCD) is non-perturbative implementation of a field theory in which QCD quantities are calculated on a discrete space-time grid. LQCD allows to obtain properties of matter in equilibrium, but there are some limitations. Lattice QCD requires fine lattice spacing to obtain precise results - therefore large computational resources are necessary. With the constant growth of computing power this problem will become less important. The second problem is that lattice simulations are possible only for baryon density $\mu_B = 0$. At $\mu_B \neq 0$, Lattice QCD breaks down because of the sign problem [6]. The μ_B is the baryonic chemical potential. It is one of the statistical-thermal model parameters.

1.2.3 The quark-gluon plasma

The new state of matter in which quarks are no longer confined is known as a *quark-gluon plasma* (QGP). The predictions coming from the discrete space-time Lattice QCD calculations reveal a phase transition from the hadronic matter to the quark-gluon plasma at the high temperatures and baryon densities. The res-

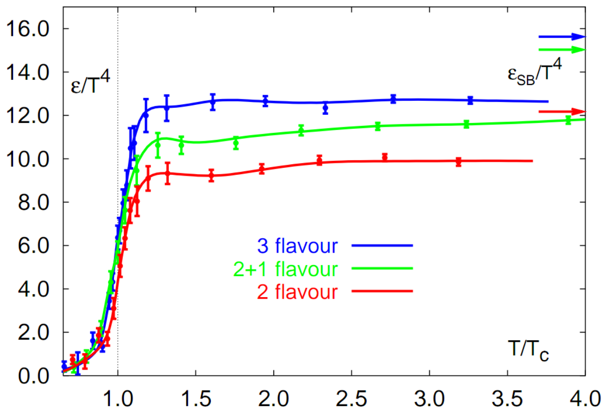

Figure 1.5: A number of degrees of freedom as a function of a temperature [7].

ults obtained from such calculations are shown on Fig. 1.5. The energy density ϵ which is divided by T^4 is a measure of number of degrees of freedom in the system. One can observe significant rise of this value, when the temperature increases past the critical value T_C. Such increase is signaling a phase transition - the formation of QGP [8]. The values of the energy densities plotted in Fig. 1.5 do not reach the Stefan-Boltzmann limit ϵ_{SB} (marked with arrows), which corresponds to an ideal gas. This can indicate some residual interactions in the system. According to the results from the RHIC[2], the new phase of matter behaves more like an ideal fluid, than like a gas [9].

One of the key questions, to which current heavy ion physics tries to find an answer is the value of a critical temperature T_C as a function of a baryon chemical potential μ_B (baryon density), where the phase transition occur. The results coming from the Lattice QCD are presented in the Fig. 1.6. The phase of

[2]Relativistic Heavy Ion Collider at Brookhaven National Laboratory in Upton, New York

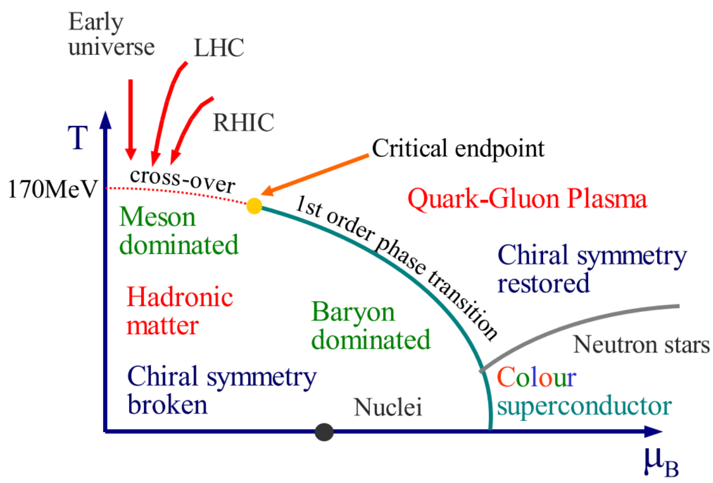

Figure 1.6: Phase diagram coming from the Lattice QCD calculations [8].

matter in which quarks and gluons are deconfined is expected to exist at large temperatures. In the region of small temperatures and high baryon densities, a different state is supposed to appear - a *colour superconductor*. The phase transition between hadronic matter and QGP is thought to be of 1^{st} order at $\mu_B \gg 0$. However as $\mu_B \to 0$ quarks' masses become significant and a sharp transition transforms into a rapid but smooth cross-over. It is believed that in Pb-Pb collisions observed at the LHC[3], the created matter has high enough temperature to be in the quark-gluon plasma phase, then cools down and converts into hadrons, undergoing a smooth transition [8].

1.3 Relativistic heavy ion collisions

1.3.1 Stages of heavy ion collision

To create the quark-gluon plasma one has to achieve high enough temperatures and baryon densities. Such conditions can be recreated in the heavy ion collisions at the high energies. The left side of the Figure 1.7 shows simplified picture of a central collision of two highly relativistic nuclei in the centre-of-mass reference frame. The colliding nuclei are presented as thin disks because of the Lorentz contraction. In the central region, where the energy density is the highest, a new state of matter - the quark-gluon plasma - is supposedly created. Afterwards, the plasma expands ad cools down, quarks combine into hadrons and their mutual interactions cease when the system reaches the *freeze-out* temperature. Subsequently, produced free hadrons move towards the detectors.

On the right side of the Figure 1.7 there is presented a space-time evolution

[3] Large Hadron Collider at CERN, Geneva

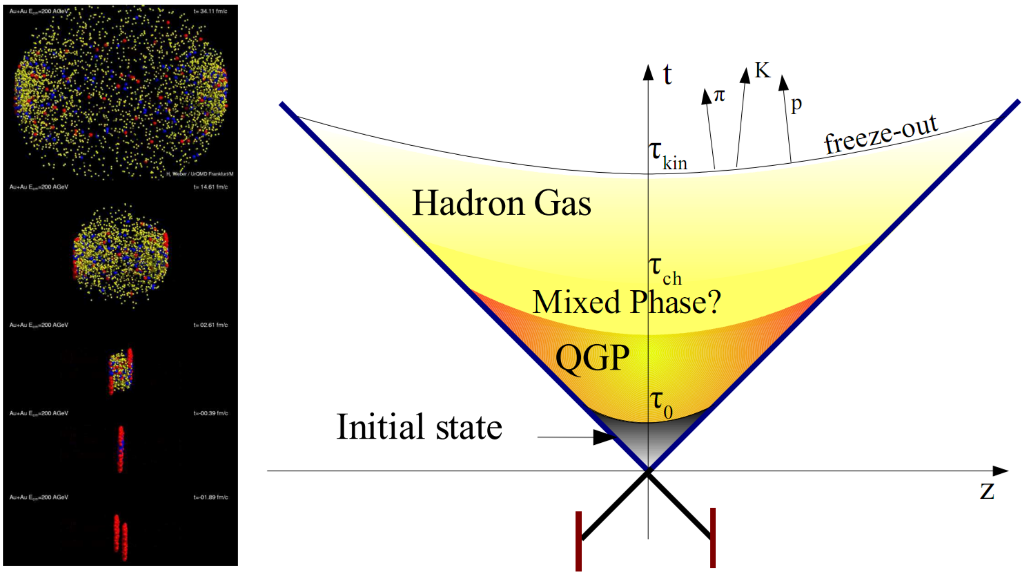

Figure 1.7: Left: stages of a heavy ion collision simulated in the UrQMD model. Right: schematic view of a heavy ion collision evolution [8].

of a collision process, plotted in the light-cone variables (z, t). The two highly relativistic nuclei are traveling basically along the light cone until they collide at the centre of diagram. Nuclear fragments emerge from the collision again along the (forward) light cone, while the matter between fragmentation zones populates the central region. This hot and dense matter is believed to be in the state of the quark-gluon plasma. There exist several frameworks to describe this transition to the QGP phase, for example: QCD string breaking, QCD parton cascades or colour glass condensate evolving into glasma and later into quark-gluon plasma [10].

String breaking – In the string picture, the nuclei pass through each other forming colour strings. This is analogous to the situation depicted in the Fig 1.2 - the colour string is created between quarks inside particular nucleons in nuclei. In the next step strings decay / fragment forming quarks and gluons or directly hadrons. This approach becomes invalid at very high energies, when the strings overlap and cannot be treated as independent objects.

Parton cascade – The parton[4] cascade model is based on the pQCD. The colliding nuclei are treated as clouds of quarks and which penetrate through each other. The key element of this method is the time evolution of the partion phase-space distributions, which is governed by a relativistic Boltzmann equation with a collision term that contains dominant perturbative QCD interations. The bottleneck of the parton cascade model is the low energies regime, where the Q^2 is too small to be described by the perturbative theory.

[4]A parton is a common name for a quark and a gluon.

Colour glass condensate – The colour glass condensate assumes, that the hadron can be viewed as a tightly packed system of interacting gluons. The saturation of gluons increases with energy, hence the total number of gluons may increase without the bound. Such a saturated and weakly coupled gluon system is called a colour glass condensate. The fast gluons in the condensate are Lorentz contracted and redistributed on the two very thin sheets representing two colliding nuclei. The sheets are perpendicular to the beam axis. The fast gluons produce mutually orthogonal colour magnetic and electric fields, that only exist on the sheets. Immediately after the collision, i.e. just after the passage of the two gluonic sheets after each other, the longitudinal electric and magnetic fields are produced forming the *glasma*. The glasma fields decay through the classical rearrangement of the fields into radiation of gluons. Also decays due to the quantum pair creations are possible. In this way, the quark-gluon plasma is produced.

Interactions within the created quark-gluon plasma bring the system into the local statistical equilibrium, hence its further evolution can be described by the relativistic hydrodynamics. The hydrodynamic expansion causes that the system becomes more and more dilute. The phase transition from the quark-gluon plasma to the hadronic gas occurs. Further expansion causes a transition from the strongly interaction hadronic gas to weakly interacting system of hadrons which move freely to the detectors. Such decoupling of hadrons is called the *freeze-out*. The freeze-out can be divided into two phases: the chemical freeze-out and the thermal one. The *chemical freeze-out* occurs when the inelastic collisions between constituents of the hadron gas stop. As the system evolves from the chemical freeze-out to the thermal freeze-out the dominant processes are elastic collisions (such as, for example $\pi + \pi \to \rho \to \pi + \pi$) and strong decays of heavier resonances which populate the yield of stable hadrons. The *thermal freeze-out* is the stage of the evolution of matter, when the strongly coupled system transforms to a weakly coupled one (consisting of essentially free particles). In other words this is the moment, where the hadrons practically stop to interact. Obviously, the temperatures corresponding to the two freeze-outs satisfy the condition

$$T_{chem} > T_{therm} \,, \tag{1.2}$$

where T_{chem} (inferred from the ratios of hadron multiplicities) is the temperature of the chemical freeze-out, and T_{therm} (obtained from the investigation of the transverse-momentum spectra) is the temperature of the thermal freeze-out [10].

1.3.2 QGP signatures

The quark-gluon plasma is a very short living and unstable state of matter. One cannot investigate the properties of a plasma and confirm its existence directly. Hence, the several experimental effects were proposed as QGP signatures, some of them have been already observed in heavy ion experiments [8]. As matter created in the heavy ions collisions is supposed to behave like a fluid, one should expect appearance of collective behaviour at small transverse momenta - so called *elliptic flow* and *radial flow*. The next signal is the temperature range obtained from the measurements of *direct photons*, which gives us information, that the system created in heavy ion collisions is far above the critical temperature obtained from the LQCD calculations. The *puzzle in the di-lepton spectrum* can be explained by the modification of spectral shape of vector mesons (mostly ρ meson) in the presence of a dense medium. This presence of a medium can also shed light on the *jet quenching* phenomenon - the suppression occurence in the high p_T domain.

Elliptic flow

In a non-central heavy ion collisions, created region of matter has an almond shape with its shorter axis in the *reaction plane* (Fig. 1.8). The pressure gradient is much larger in-plane rather than out-of-plane. This causes larger acceleration and transverse velocities in-plane rather than out-of-plane. Such differences can

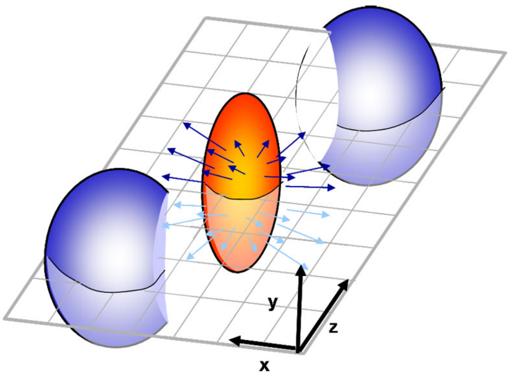

Figure 1.8: Overlapping region which is created in heavy ion collisions has an almond shape. Visible x-z plane is a *reaction plane*. The x-y plane is a *transverse plane*. The z is a direction of the beam [11].

be investigated by studying the distribution of particles with respect to the reaction plane orientation [12]:

$$E\frac{d^3N}{dp^3} = \frac{1}{2\pi}\frac{d^2N}{p_T dp_T dy}(1 + 2v_1\cos(\phi) + 2v_2\cos(2\phi) + ...) \,, \tag{1.3}$$

where ϕ is the angle between particle transverse momentum p_T (a momentum projection on a transverse plane) and the reaction plane, N is a number of particles and E is an energy of a particle. The y variable is a *rapidity* defined as:

$$y = \frac{1}{2}\ln\left(\frac{E + p_L}{E - p_L}\right) \,, \tag{1.4}$$

where p_L is a longitudinal component of a momentum (paralel to the beam direction). The v_n coefficients indicate the shape of a system. For the most central collisions (b = 0 - see Fig. 1.9) all coefficients vanish $\bigwedge_{n \in N_+} v_n = 0$ (the overlapping region has the spherical shape). The Fourier series elements in the parentheses

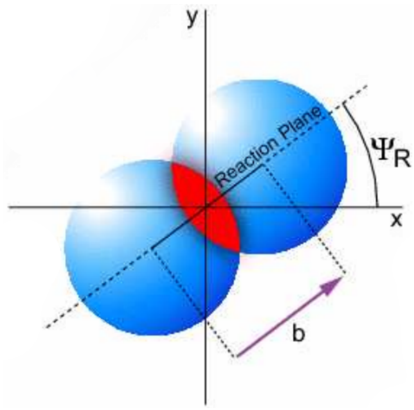

Figure 1.9: Cross-section of a heavy ion collision in a transverse plane. Ψ_R is an angle between transverse plane and the reaction plane. The *b* parameter is an *impact parameter* - a distance between centers of nuclei during a collision. An impact parameter is related with the centrality of a collision and a volume of the quark-gluon plasma [12].

in Eq. 1.3 represent different kinds of a flow. The first value: "1" represents the *radial flow* - an isotropic flow in every direction. Next coefficient v_1 is responsible for *direct flow*. The v_2 coefficient is a measure of elliptic anisotropy (*elliptic flow*). The v_2 has to build up in the early stage of a collision - later the system becomes too dilute: space asymmetry and the pressure gradient vanish. Therefore the observation of elliptic flow means that the created matter was in fact a strongly interacting matter.

The v_2 coefficient was measured already at CERN SPS, LHC and RHIC. For the first time hydrodynamics successfully described the collision dynamics as the measured v_2 reached hydrodynamic limit (Fig. 1.10). As expected, there is a mass ordering of v_2 as a function of p_T (lower plot in the Fig. 1.10) with pions having the largest and protons the smallest anisotropy. In the upper plots in the Fig. 1.10 there is a v_2 as a function of transverse kinetic energy. The left plot shows the two unversal trend lines for baryons and mesons. After the scaling of v_2 and the kinetic energy by the number of valence quarks, all of the hadrons follow the same universal curve. Those plots show that strong collectivity is observed in heavy ion collisions.

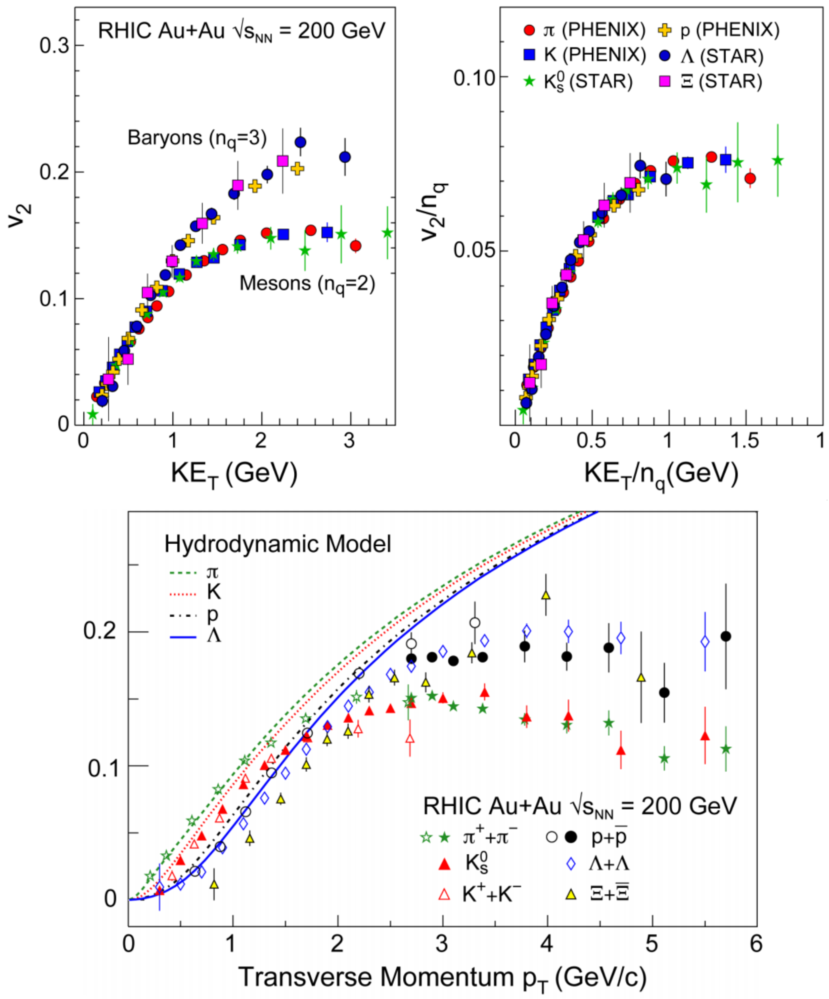

Figure 1.10: *Lower:* The elliptic flow v_2 follows the hydrodynamical predictions for an ideal fluid perfectly. Note that $> 99\%$ of all final hadrons have $p_T < 1.5$ GeV/c. *Upper left:* The v_2 plotted versus transverse kinetic energy $KE_T = m_T - m_0 = \sqrt{p_T^2 + m_0^2} - m_0$. The v_2 follows different universal curves for mesons and baryons. *Upper right:* When scaled by the number of valence quarks, the v_2 follows the same universal curve for all hadrons and for all values of scaled transverse kinetic energy [13].

Transverse radial flow

Elliptic flow described previously is caused by the pressure gradients which must also produce a more simple collective behaviour of matter - a movement inside-out, called radial flow. Particles are pushed to higher momenta and they move away from the center of the collision. A source not showing collective behaviour, like pp collisions, produces particle spectra that can be fitted by a power-law [8]:

$$\frac{1}{2\pi p_T}\frac{d^2N}{dp_T d\eta} = C\left(1+\frac{p_T}{p_0}\right) . \tag{1.5}$$

The η variable is a *pseudorapidity* defined as follows:

$$\eta = \frac{1}{2}\ln\left(\frac{p+p_L}{p-p_L}\right) = -\ln\left(\frac{\theta}{2}\right) , \tag{1.6}$$

where θ is an emission angle $\cos\theta = p_L/p$.

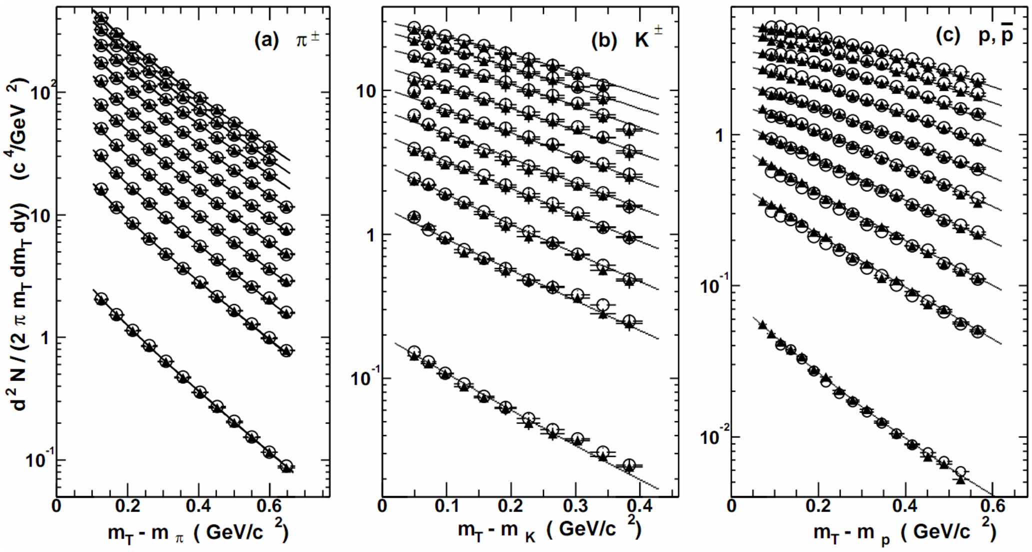

Figure 1.11: Invariant yield of particles versus transverse mass $m_T = \sqrt{p_T^2 + m_0^2}$ for $\pi^{\pm}$, $K^{\pm}$, p and $\bar{p}$ at mid-rapidity for p+p collisions (bottom) and Au+Au events from 70-80% (second bottom) to 0-5% (top) centrality [14].

The hydrodynamical expansion of a system gives the same flow velocity kick for different kind of particles - ones with bigger masses will gain larger p_T boost. This causes increase of the yield of particles with larger transverse momenta. In the invariant yield plots one can observe the decrease of the slope parameter, especially for the heavier hadrons. This is presented in the Fig. 1.11. The most affected spectra are ones of kaons (b) and protons (c). One can notice decrease of the slope parameter for heavy ion collisions (plots from second bottom to top) comparing to the proton-proton collisions (bottom ones), where no boost from radial flow should occur [8].

Direct photons

The direct photons are photons, which are not coming from the final state hadrons decays. Their sources can be various interaction from charged particles created in the collision, either at the partonic or at the hadronic level. Direct photons are considered to be an excellent probe of the early stage of the collision. This is because their mean free path is very large to the created system in the collision. Thus photons created at the early stage leave the system without suffering any interaction and retain information about this stage, in particular about its temperature.

One can distinguish two kinds of direct photons: *thermal* and *prompt*. Thermal photons can be emitted from the strong processes in the quark-gluon plasma involving quarks and gluons or hot hadronic matter (e.g. processes: $\pi\pi \rightarrow \rho\gamma$, $\pi\rho \rightarrow \pi\gamma$). Thermal photons can be observed in the low p_T region. Prompt photons are believed to come from "hard" collisions of initial state partons belonging to the colliding nuclei. The prompt photons can be described using the pQCD. They will dominate the high p_T region. The analysis of transverse momentum of spectra of direct photons revealed, that the temperature of the source of thermal photons produced in heavy ion collisions at RHIC is in the range 300-600 MeV (Fig. 1.12). Hence the direct photons had to come from a system whose temperature is far above from the critical temperature for QGP creation.

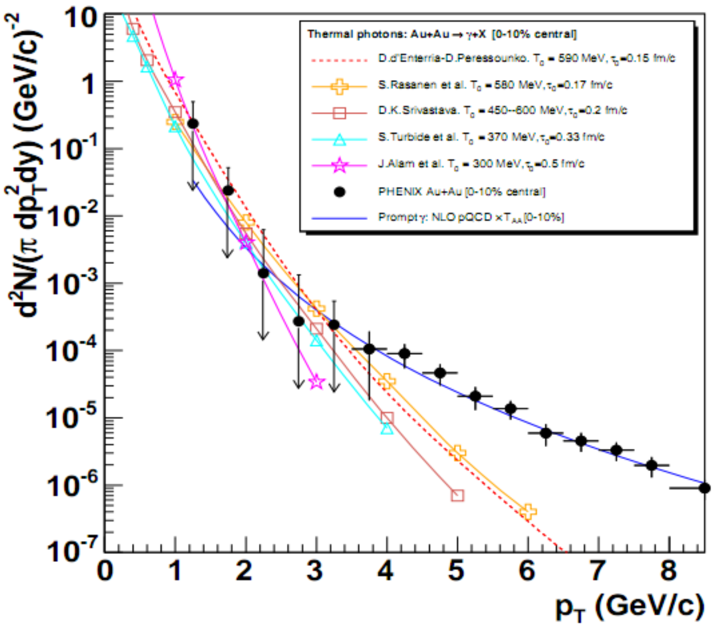

Figure 1.12: Thermal photons spectra for the central Au+Au collisions at $\sqrt{s_{NN}} = 200$ GeV at computed within different hydrodynamical models compared with the pQCD calculations (solid line) and experimental data from PHENIX (black dots) [15].

Puzzle in di-lepton mass spectrum

The invariant mass spectra (Fig. 1.13) of lepton pairs reveal many peaks corresponding to direct decays of various mesons into a lepton pair. The continuous background in this plot is caused by the decays of hadrons into more than two leptons (including so-called *Dalitz decays* into a lepton pair and a photon). Particular hadron decay channels, which contribute to this spectrum are shown

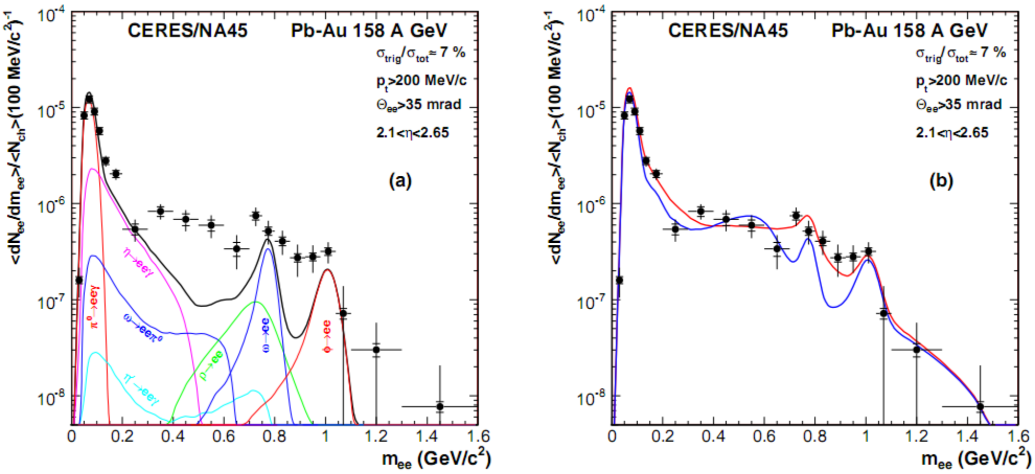

Figure 1.13: Left: Invariant mass spectrum of e^{+}-e^{-} pairs in Pb+Au collisions at 158A GeV compared to the sum coming from the hadron decays predictions. Right: The expectations coming from model calculations assuming a dropping of the ρ mass (blue) or a spread of the ρ width in the medium (red) [16].

in the Fig. 1.13 with the coloured lines and their sum with the black one. The sum (called *the hadronic cocktail*) of various components describes experimental spectra coming from the simple collisions (like p+p or p+A) quite well with the statistical and systematical uncertainties [9]. This situation is different considering more complicated systems i.e. A+A. Spectra coming from Pb+Au collisions are presented on the plots in the Fig. 1.13. The "hadronic cocktail" does not describe the data, in the mass range between the π and the ρ mesons a significant excess of electron pairs over the calculated sum is observed. Theoretical explanation of this phenomenon assumes modification of the spectral shape of vector mesons in a dense medium. Two different interpretations of this increase were proposed: a decrease of meson mass with the medium density and increase of the meson width in the dense medium. In principle, one could think of simultaneous occurrence of both effects: mass shift and resonance broadening. Experimental results coming from the CERES disfavour the mass shift hypothesis indicating only broadening of resonance peaks (Fig. 1.13b) [9].

Jet quenching

A jet is defined as a group of particles with close vector momenta and high energies. It has its beginning when the two partons are going in opposite directions and have energy big enough to produce new quark-antiquark pair and then radiate gluons. This process can be repeated many times and it results in two back-to-back jets of hadrons. It has been found that jets in the opposite hemisphere (*away-side jets*) show a very different pattern in d+Au and Au+Au collisions. This is shown in the azimuthal correlations in the Fig. 1.14. In d+Au collisions, like in p+p, a pronounced away-side jet appears around $\Delta\phi = \pi$, exactly opposite to the trigger jet, what is typical for di-jet events. In central Au+Au collisions the away jet is suppressed. When the jet has its beginning near the surface of the quark-

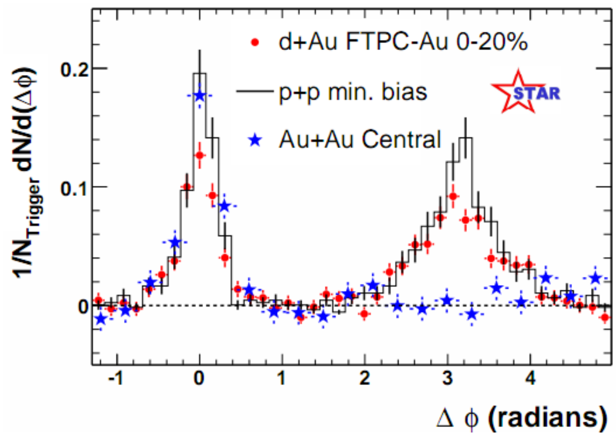

Figure 1.14: Azimuthal angle difference $\Delta\phi$ distributions for different colliding systems at $\sqrt{s_{NN}}$ = 200 GeV. Transverse momentum cut: $p_T > 2$ GeV. For the Au+Au collisions the away-side jet is missing [17].

qluon plasma, one of the jets (*near-side jet*) leaves the system almost without any interactions. This jet is visible on the correlation plot as a high peak at $\Delta\phi = 0$. However, the jet moving towards the opposite direction has to penetrate a dense medium. The interaction with the plasma causes energy dissipation of particles and is visible on an azimuthal correlation plot as disappearance of the away-side jet [9].

Chapter 2

Therminator model

THERMINATOR [18] is a Monte Carlo event generator designed to investigate the particle production in the relativistic heavy ion collisions. The functionality of the code includes a generation of the stable particles and unstable resonances at the chosen hypersurface model. It performs the statistical hadronization which is followed by space-time evolution of particles and the decay of resonances. The key element of this method is an inclusion of a complete list of hadronic resonances, which contribute very significantly to the observables. The second version of THERMINATOR [19] comes with a posibility to incorporate any shape of freeze-out hypersurface and the expansion velocity field, especially those generated externally with various hydrodynamic codes.

2.1 (3+1)-dimensional viscous hydrodynamics

Most of the relativistic viscous hydrodynamic calculations are done in (2+1)-dimensions. Such simplification assumes boost-invariance of a matter created in a collision. Experimental data reveals that no boost-invariant region is formed in the collisions [20]. Hence, for the better description of created system a (3+1)-dimensional model is required.

In the four dimensional relativistic dynamics one can describe a system using a space-time four-vector $x^\nu = (ct, x, y, z)$, a velocity four-vector $u^\nu = \gamma(c, v_x, v_y, v_z)$ and a energy-momentum tensor $T^{\mu\nu}$. The particular components of $T^{\mu\nu}$ have a following meaning:

- T^{00} - an energy density,
- $cT^{0\alpha}$ - an energy flux across a surface x^α,
- $T^{\alpha 0}$ - an α-momentum flux across a surface x^α multiplied by c,
- $T^{\alpha\beta}$ - components of momentum flux density tensor,

where $\gamma = (1 - v^2/c^2)^{-1/2}$ is Lorentz factor and $\alpha, \beta \in \{1, 2, 3\}$. Using u^ν one can express $T^{\mu\nu}$ as follows [21]:

$$T_0^{\mu\nu} = (e + p)u^\mu u^\nu - pg^{\mu\nu} \tag{2.1}$$

where e is an energy density, p is a pressure and $g^{\mu\nu}$ is an inverse metric tensor:

$$g^{\mu\nu} = \begin{bmatrix} 1 & 0 & 0 & 0 \\ 0 & -1 & 0 & 0 \\ 0 & 0 & -1 & 0 \\ 0 & 0 & 0 & -1 \end{bmatrix}. \tag{2.2}$$

The presented version of energy-momentum tensor (Eq. 2.1) can be used to describe dynamics of a perfect fluid. To take into account influence of viscosity, one has to apply the following corrections coming from shear $\pi^{\mu\nu}$ and bulk Π viscosities [22]:

$$T^{\mu\nu} = T_0^{\mu\nu} + \pi^{\mu\nu} + \Pi(g^{\mu\nu} - u^\mu u^\nu). \tag{2.3}$$

The stress tensor $\pi^{\mu\nu}$ and the bulk viscosity Π are solutions of dynamical equations in the second order viscous hydrodynamic framework [21]. The comparison of hydrodynamics calculations with the experimental results reveal, that the shear viscosity divided by entropy η/s has to be small and close to the AdS/CFT estimate η/s = 0.08 [22, 23]. The bulk viscosity over entropy value used in calculations is ζ/s = 0.04 [22].

When using $T^{\mu\nu}$ to describe system evolving close to local thermodynamic equilibrium, relativistic hydrodynamic equations in a form of:

$$\partial_\mu T^{\mu\nu} = 0 \tag{2.4}$$

can be used to describe the dynamics of the local energy density, pressure and flow velocity.

Hydrodynamic calculations are starting from the Glauber [1] model initial conditions. The collective expansion of a fluid ends at the freeze-out hypersurface. That surface is usually defined as a constant temperature surface, or equivalently as a cut-off in local energy density. The freeze-out is assumed to occur at the temperature T = 140 MeV.

2.2 Statistical hadronization

Statistical description of heavy ion collision has been successfully used to describe quantitatively *soft* physics, i.e. the regime with the transverse momentum not exceeding 2 GeV. The basic assumption of the statistical approach of evolution of the quark-gluon plasma is that at some point of the

[1]The Glauber Model is used to calculate "geometrical" parameters of a collision like an impact parameter, number of participating nucleons or number of binary collisions.

space-time evolution of the fireball, the thermal equilibrium is reached. When the system is in the thermal equilibrium the local phase-space densities of particles follow the Fermi-Dirac or Bose-Einstein statistical distributions. At the end of the plasma expansion, the freeze-out occurs. The freeze-out model incorporated in the THERMINATOR model assumes, that chemical and thermal freeze-out occur at the same time.

2.2.1 Cooper-Frye formalism

The result of the hydrodynamic calculations is the freeze-out hypersurface Σ^{μ}. A three-dimensional element of the surface is defined as [19]

$$d\Sigma_{\mu} = \epsilon_{\mu\alpha\beta\gamma} \frac{\partial x^{\alpha}}{\partial \alpha} \frac{\partial x^{\beta}}{\partial \beta} \frac{\partial x^{\gamma}}{\partial \gamma} d\alpha d\beta d\gamma, \tag{2.5}$$

where $\epsilon_{\mu\alpha\beta\gamma}$ is the Levi-Civita tensor and the variables $\alpha, \beta, \gamma \in \{1, 2, 3\}$ are used to parametrize the three-dimensional freeze-out hypersurface in the Minkowski four-dimensional space. The Levi-Civita tensor is equal to 1 when the indices form an even permutation (eg. ϵ_{0123}), to -1 when the permutation is odd (e.g. ϵ_{2134}) and has a value of 0 if any index is repeated. Therefore [19],

$$d\Sigma_0 = \begin{vmatrix} \frac{\partial x}{\partial \alpha} & \frac{\partial x}{\partial \beta} & \frac{\partial x}{\partial \gamma} \\ \frac{\partial y}{\partial \alpha} & \frac{\partial y}{\partial \beta} & \frac{\partial y}{\partial \gamma} \\ \frac{\partial z}{\partial \alpha} & \frac{\partial z}{\partial \beta} & \frac{\partial z}{\partial \gamma} \end{vmatrix} d\alpha d\beta d\gamma \tag{2.6}$$

and the remaining components are obtained by cyclic permutations of t, x, y and z.

One can obtain the number of hadrons produced on the hypersurface Σ^{μ} from the Cooper-Frye formalism. The following integral yields the total number of created particles [19]:

$$N = (2s+1) \int \frac{d^3p}{(2\pi)^3 E_p} \int d\Sigma_{\mu} p^{\mu} f(p_{\mu} u^{\mu}) \ , \tag{2.7}$$

where $f(p_{\mu}u^{\mu})$ is the phase-space distribution of particles (for stable ones and resonances). One can simply derive from Eq. 2.7, the dependence of the momentum density [24]:

$$E \frac{d^3N}{dp^3} = \int d\Sigma_{\mu} f(p_{\mu}u^{\mu}) p^{\mu} \ . \tag{2.8}$$

The momentum distribution f contains non-equilibrium corrections:

$$f = f_0 + \delta f_{shear} + \delta f_{bulk} \ , \tag{2.9}$$

where

$$f_0(p_{\mu}u^{\mu}) = \left\{ \exp\left[\frac{p_{\mu}u^{\mu} - (B\mu_B + I_3\mu_{I_3} + S\mu_S + C\mu_C)}{T} \right] \pm 1 \right\}^{-1} \tag{2.10}$$

In case of fermions, in the Eq. 2.10 there is a plus sign and for bosons, minus sign respectively. The thermodynamic quantities appearing in the $f_0(\cdot)$ are T - temperature, μ_B - baryon chemical potential, μ_{I_3} - isospin chemical potential, μ_S - strange chemical potential, μ_C - charmed chemical potential and the s is a spin of a particle. The hydrodynamic calculations yield the flow velocity at freeze-out as well as the stress and bulk viscosity tensors required to calculate non-equilibrium corrections to the momentum distribution used in Eq. 2.7. The term coming from shear viscosity has a form [22]

$$\delta f_{shear} = f_0(1 \pm f_0)\frac{1}{2T^2(e+p)}p^\mu p^\nu \pi_{\mu\nu} \tag{2.11}$$

and bulk viscosity

$$\delta f_{bulk} = C f_0(1 \pm f_0)\left(\frac{(u^\mu p_\mu)^2}{3u^\mu p_\mu} - c_s^2 u^\mu p_\mu\right)\Pi \tag{2.12}$$

where c_s is sound velocity and

$$\frac{1}{C} = \frac{1}{3}\frac{1}{(2\pi)^3}\sum_{hadrons}\int d^3p\frac{m^2}{E}f_0(1 \pm f_0)\left(\frac{p^2}{3E} - c_s^2 E\right) . \tag{2.13}$$

The equations presented above are directly used in the `THERMINATOR` to generate the primordial hadrons (created during freeze-out) with the Monte-Carlo method. Resonances produced in this way, propagate and decay, in cascades if necessary. For every generated particle, its origin point either on a hypersurface or is associated with the point of the decay of the parent particle. This information is kept in the simulation due to its importance for the femtoscopic analysis.

Chapter 3

Particle interferometry

Two-particle interferometry (also called *femtoscopy*) gives a possibility to investigate space-time characteristics of the particle-emitting source created in heavy ion collisions. Through the study of particle correlations, their momentum distributions can be used to obtain information about the spatial extent of the created system. Using this method, one can measure sizes of the order of 10^{-15} m and time of the order of 10^{-23} s.

3.1 HBT interferometry

In the 1956 Robert Hanbury Brown and Richard Q. Twiss proposed a method which through analysis of interference between photons allowed to investigate angular dimensions of stars. The most important result from the Hanbury-Brown-Twiss experiments is that two indistinguishable particles can produce an interference effect. There is almost no difference between normal interferometry and HBT method, except that the latter one does not take into account information about phase shift of registered particles. At the beginning this method was used in astronomy for photon interference, but this effect can be used also to measure extent of any emitting source. This method was adapted to heavy ion collisions to investigate dimensions of a system created in those collisions by studying correlations of identical particles [25]. The main difference between HBT method in astronomy and femtoscopy is that the first one is based on space-time HBT correlations and the latter one uses momentum correlations. The momentum correlations yield the space-time picture of the source, whereas the space-time HBT correlations provide the characteristic relative momenta of emitted photons, which gives the angular size of the star without the knowledge of its radius and lifetime [10].

3.2 Theoretical approach

Intensity interferometry in heavy ion physics uses similar mathematical formalism as the astronomy HBT measurement. Through the measurement of correlation between particles as a function of their relative momentum one can deduce the average separation between emitting sources.

3.2.1 Conventions used

In heavy ion collisions to describe particular directions, components of momentum and location of particles, one uses naming convention called the Bertsch-Pratt coordinate system. This system is presented in the Fig. 3.1. The three dir-

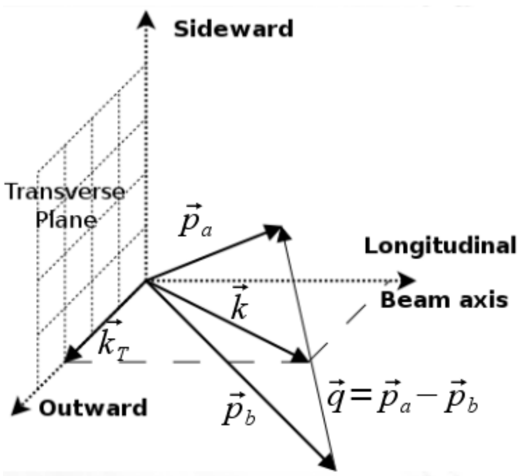

Figure 3.1: Bertsch-Pratt direction naming convention used in heavy ion collision.

ections are called *longitudinal*, *outward* and *sideward*. The longitudinal direction is parallel to the beam axis. The plane perpendicular to the beam axis is called a *transverse plane*. A projection of a particle pair momentum $\mathbf{k} = (\mathbf{p}_a + \mathbf{p}_b)/2$ on a transverse plane (a *transverse momentum* $\mathbf{k}_T$) determines *outward* direction: $(\mathbf{k})_{out} = \mathbf{k}_T$. A direction perpendicular to the longitudinal and outward is called *sideward*.

A particle pair is usually described using two coordinate systems. The first one, *Longitudinally Co-Moving System* (**LCMS**) is moving along the particle pair with the longitudinal direction, in other words, the pair longitudinal momentum vanishes: $(\mathbf{p}_a)_{long} = -(\mathbf{p}_b)_{long}$. The second system is called *Pair Rest Frame* (**PRF**). In the PRF the centre of mass rests: $\mathbf{p}_a = -\mathbf{p}_b$. Variables which are expressed in the PRF are marked with a star (e.g. $\mathbf{k}^*$).

The transition of space-time coordinates from LCMS to PRF is simply a boost along the outward direction, with the transverse velocity of the pair $\beta_T = (\mathbf{v}/c)_{out}$ [25]:

$$\begin{aligned} r^*_{out} &= \gamma_t(r_{out} - \beta_T \Delta t) && (3.1)\\ r^*_{side} &= r_{side} && (3.2)\\ r^*_{long} &= r_{long} && (3.3)\\ \Delta t^* &= \gamma_T(\Delta t - \beta_T r_{out}) \ , && (3.4) \end{aligned}$$

where $\gamma_T = (1-\beta_T^2)^{-1/2}$ is the Lorentz factor. However, in calculations performed in this work the equal time approximation is used, which assumes that particles in a pair were produced at the same time in PRF - the Δt^* is neglected.

The most important variables used to describe particle pair are their total momentum $\mathbf{P} = \mathbf{p}_a + \mathbf{p}_b$ and relative momentum $\mathbf{q} = \mathbf{p_a} - \mathbf{p_b}$. In the PRF one has $\mathbf{q} = 2\mathbf{k}^*$, where $\mathbf{k}^*$ is a momentum of the first particle in PRF.

3.2.2 Two particle wave function

Let us consider two identical particles with momenta $\mathbf{p_1}$ and $\mathbf{p_2}$ emitted from space points $\mathbf{x_1}$ and $\mathbf{x_2}$. Those emitted particles can be treated as two incoherent waves. If the particles are identical, they are also indistinguishable, therefore one

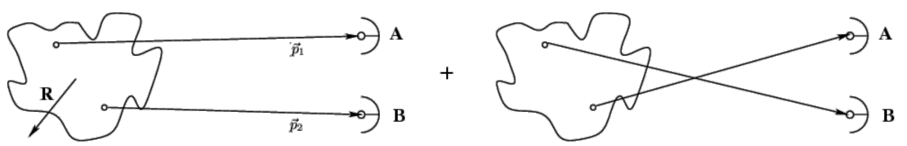

Figure 3.2: The pair wave function is a superposition of all possible states. In case of particle interferometry it includes two cases: particles with momenta p_1, p_2 registered by detectors *A*, *B* and p_1, p_2 registered by *B*, *A* respectively.

has also take into account the scenario, where the particle with momentum $\mathbf{p_1}$ is emitted from $\mathbf{x_2}$ and particle $\mathbf{p_2}$ from $\mathbf{x_1}$ (Fig. 3.2). In such case, the wave function describing behaviour of a pair has to contain both components [8]:

$$\Psi_{ab}(\mathbf{q}) = \frac{1}{\sqrt{2}}\left[\exp(-i\mathbf{p_1}\mathbf{x_1} - i\mathbf{p_2}\mathbf{x_2}) \pm \exp(-i\mathbf{p_2}\mathbf{x_1} - i\mathbf{p_1}\mathbf{x_2})\right] \ . \qquad (3.5)$$

A two particle wave function of identical bosons is symmetric ("+" sign in Eq. 3.5) and in case of identical fermions - antisymmetric ("-" sign). This anti-symmetrization or symmetrization implies the correlation effect coming from the Fermi-Dirac or Bose-Einstein statistics accordingly.

To provide full description of a system consisting of two charged hadrons, one has to include in the wave function besides quantum statistics also Coulomb and strong Final State Interactions. Considering identical particles systems, the quantum statistics is a main source of a correlation. Hence, in case of space-time analysis of particle emitting source, effects coming from the Coulomb and Strong interactions can be neglected.

3.2.3 Source emission function

To describe particle emitting source, one uses a single emission function [25]:

$$S_A(\mathbf{x}_1, \mathbf{p}_1) = \int S(\mathbf{x}_1, \mathbf{p}_1, \mathbf{x}_2, \mathbf{p}_2, ..., \mathbf{x}_N, \mathbf{p}_N) d\mathbf{x}_2 d\mathbf{p}_2 ... d\mathbf{x}_N d\mathbf{p}_N \tag{3.6}$$

and a two-particle one:

$$S_{AB}(\mathbf{x}_1, \mathbf{p}_1, \mathbf{x}_2, \mathbf{p}_2) = \int S(\mathbf{x}_1, \mathbf{p}_1, \mathbf{x}_2, \mathbf{p}_2, ..., \mathbf{x}_N, \mathbf{p}_N) d\mathbf{x}_3 d\mathbf{p}_3 ... d\mathbf{x}_N d\mathbf{p}_N \ . \tag{3.7}$$

Emission function $S(\cdot)$ can be interpreted as a probability to emit a particle, or a pair of particles from a given space-time point with a given momentum. In principle, the source emission function should encode all physics aspects of the particle emission process i.e. the symmetrization for bosons and fermions, as well as the two-body and many body Final State Interactions. Instead of this, one assume that each particle's emission process is independent - the interaction between final-state particles after their creation is independent from their emission process. The assumption of this independence allows to construct two-particle emission function from single particle emission functions via a convolution [25]:

$$S(\mathbf{k}^*, \mathbf{r}^*) = \int S_A(\mathbf{p}_1, \mathbf{x}_1) S_B(\mathbf{p}_2, \mathbf{x}_2) \delta \left[\mathbf{k}^* - \frac{\mathbf{p}_1 + \mathbf{p}_2}{2} \right] \delta \left[\mathbf{r}^* - (\mathbf{x}_1 + \mathbf{x}_2) \right] \times d^4\mathbf{x}_1 d^4\mathbf{x}_2 d^4\mathbf{x}_1 d^3\mathbf{p}_1 d^3\mathbf{p}_2 \tag{3.8}$$

In case of identical particles, ($S_A = S_B$) several simplifications can be made. A convolution of the two same Gaussian distributions is also a Gaussian distribution with σ multiplied by $\sqrt{2}$. Femtoscopy can give information only about two-particle emission function, but when considering Gaussian distribution as a source function in Eq. 3.8, one can obtain a σ of a single emission function from a two-particle emission function. The Eq. 3.8 is not reversible - an information about $S_A(\cdot)$ cannot be derived from $S_{AB}(\cdot)$. An exception from this rule is a Gaussian source function, hence it is often used in femtoscopic calculations. Considering pairs of identical particles, an emission function is assumed to be described by the following equation in the Pair Rest Frame [25]:

$$S_{1D}^{PRF}(\mathbf{r}^*) = \exp\left(-\frac{{r^*_{out}}^2 + {r^*_{side}}^2 + {r^*_{long}}^2}{4{R_{inv}}^2} \right) \ . \tag{3.9}$$

To change from the three-dimensional variables to the one-dimensional variable one requires introduction of the proper Jacobian r^{*2}:

$$\boxed{S_{1D}^{PRF}(r^*) = r^{*2} \exp\left(-\frac{r^{*2}}{4{R_{inv}}^2} \right)} \ . \tag{3.10}$$

The “4” in the denominator before the “standard deviation” R_{inv} in the Gaussian distribution comes from the convolution of the two Gaussian distributions, which multiplies the R_{inv} by a factor of $\sqrt{2}$.

A more complex form of emission function was used by all RHIC and SPS experiments in identical pion femtoscopy:

$$\boxed{S_{3D}^{LCMS}(\mathbf{r}) = \exp\left(-\frac{r_{out}^2}{4{R_{out}}^2} - \frac{r_{side}^2}{4{R_{side}}^2} - \frac{r_{long}^2}{4{R_{long}}^2}\right)} . \tag{3.11}$$

The main difference of this source function is that it has three different and independent widths R_{out}, R_{side}, R_{long} and they are defined in the LCMS, not in PRF. Unlike in PRF, in LCMS an equal-time approximation is not used. For identical particles this is not a problem - only Coulomb interaction inside a wave function depends on Δt.

Relationship between one-dimensional and three-dimensional source sizes

Up to now, most of femtoscopic measurements were limited only to averaged source size R_{av}^L (the letter “L” in superscript stands for LCMS):

$$S_{1D}^{LCMS}(\mathbf{r}) = \exp\left(-\frac{{r_{out}}^2 + {r_{side}}^2 + {r_{long}}^2}{2{R_{av}^L}^2}\right) . \tag{3.12}$$

The relationship between between $S_{1D}^{LCMS}(\cdot)$ and $S_{3D}^{LCMS}(\cdot)$ is given by:

$$\begin{aligned} S_{3D}^{LCMS}(r) = \int \exp\left(-\frac{r_{out}^2}{2{R_{out}^L}^2} - \frac{r_{side}^2}{2{R_{side}^L}^2} - \frac{r_{long}^2}{2{R_{long}^L}^2}\right) \\ \times\, \delta\left(r - \sqrt{r_{out}^2 + r_{side}^2 + r_{long}^2}\right) dr_{out} dr_{side} dr_{long} . \end{aligned} \tag{3.13}$$

The one-dimensional source size corresponding to the three-dimensional one can be approximated by the following form:

$$S_{1D}^{LCMS}(r) = r^2 \exp\left(-\frac{r^2}{2{R_{av}^L}^2}\right) . \tag{3.14}$$

The equation above assumes that $R_{out}^L = R_{side}^L = R_{long}^L$ hence $R_{av}^L = R_{out}^L$. If this condition is not satisfied, one can not give explicit mathematical relation between one-dimensional and three-dimensional source sizes. However, for realistic values of R (i.e. for similar values of R_{out}, R_{side}, R_{long}), the S_{3D}^{LCMS} from Eq. 3.13 is not very different from Gaussian distribution and can be well approximated by Eq. 3.13.

A deformation of an averaged source function in case of big differences in R_{out}, R_{side}, R_{long} is presented in the Fig. 3.3. A three-dimensional Gaussian distribution with varying widths was averaged into one-dimensional function using

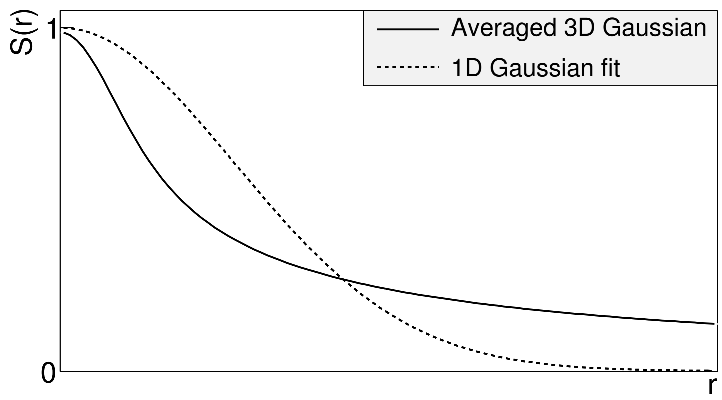

Figure 3.3: An averaged three-dimensional Gaussian source function with different widths was averaged into one-dimensional function. To illustrate deformations, one-dimensional Gaussian distribution was fitted.

the Eq. 3.13. Afterwards, an one-dimensional Gaussian distribution was fitted. One can notice a heavy tail of an averaged distribution in long r region, which makes an approximation using one-dimensional distribution in this case quite inaccurate.

Using Eq. 3.13 and Eq. 3.14 one can obtain a relation between one-dimensional width and the three-dimensional ones. Through numerical calculations one can find the following approximate relation [25]:

$$\boxed{R^L_{av} = \sqrt{\left({R^L_{out}}^2 + {R^L_{side}}^2 + {R^L_{long}}^2\right)\Big/3}} \, . \tag{3.15}$$

This equation does not depend on the pair velocity, hence it is valid in the LCMS and PRF.

3.2.4 Theoretical correlation function

The fundamental object in a particle interferometry is a correlation function. The correlation function is defined as:

$$C(\mathbf{p}_a, \mathbf{p}_b) = \frac{P_2(\mathbf{p}_a, \mathbf{p}_b)}{P_1(\mathbf{p}_a)P_1(\mathbf{p}_b)} \, , \tag{3.16}$$

where P_2 is a conditional probability to observe a particle with momentum $\mathbf{p}_b$ if particle with momentum $\mathbf{p}_b$ was also observed. A P_1 is a probability to observe a particle with a given momentum. The relationship between source emission function, pair wave function and the correlation function is described by the following equation:

$$C(\mathbf{p}_1, \mathbf{p}_2) = \int S_{AB}(\mathbf{p}_1, \mathbf{x}_1, \mathbf{p}_2, \mathbf{x}_2)|\Psi_{AB}|^2 d^4\mathbf{x}_1 d^4\mathbf{x}_2 \tag{3.17}$$

Substituting the one-dimensional emission function (Eq. 3.10) into the integral above yields the following form of correlation function in PRF:

$$\boxed{C(q) = 1 + \lambda \exp\left(-R_{inv}^2 q^2\right)} \tag{3.18}$$

where q is a momentum difference between two particles. When using the three-dimensional emission function (Eq. 3.11) one gets the following correlation function defined in the LCMS:

$$\boxed{C(\mathbf{q}) = 1 + \lambda \exp\left(-R_{out}^2 q_{out}^2 - R_{side}^2 q_{side}^2 - R_{long}^2 q_{long}^2\right)} \tag{3.19}$$

where q_{out}, q_{side}, q_{long} are $\mathbf{q}$ components in the outward, sideward and longitudinal direction. The λ parameter in the equations above determines correlation strength. The lambda parameter has values in the range $\lambda \in [-0.5, 1]$ and it depends on a pair type. In case of pairs of identical bosons (like π-π or K-K) the lambda parameter $\lambda \to 1$. For identical fermions (e.g. p-p) $\lambda \to$ -0.5. Values of λ observed experimentally are lower than 1 (for bosons) and greater than -0.5 (for fermions). There are few explanations to this effect: detector efficiencies, inclusion of misidentified particles in a used sample or inclusion of non-correlated pairs (when one or both particles come from e.g. long-lived resonance). The analysis carried out in this work uses data from a model, therefore the detector efficiency and particle purity is not taken into account [25].

3.2.5 Spherical harmonics decomposition of a correlation function

Results coming from an analysis using three-dimensional correlation function in Cartesian coordinates are quite difficult to visualize. To do that, one usually performs a projection into a one dimension in outward, sideward and longitudinal directions. One may loose important information about a correlation function in this procedure, because it gives only a limited view of the full three-dimensional structure. Recently, a more advanced way of presenting correlation function - a spherical harmonics decomposition, was proposed. The three-dimensional correlation function is decomposed into an infinite set of components in a form of one-dimensional histograms $C_l^m(q)$. In this form, a correlation function is defined as a sum of a series [26]:

$$C(\mathbf{q}) = \sum_{l,m} C_l^m(q) Y_l^m(\theta, \phi) \; , \tag{3.20}$$

where $Y_l^m(\theta, \phi)$ is a spherical harmonic function. Spherical harmonics are an orthogonal set of solutions to the Laplace's equation in spherical coordinates Hence, in this approach, a correlation function is defined as a function of q, θ and ϕ. To obtain C_l^m coefficients in the series, one has to calculate the following integral:

$$C_l^m(q) = \int_\Omega C(q, \theta, \phi) Y_l^m(\theta, \phi) d\Omega \; , \tag{3.21}$$

where Ω is a full solid angle.

Spherical harmonics representation has several important advantages. The main advantage of this decomposition is that it requires less statistics than traditional analysis performed in Cartesian coordinates. Another one is that it encodes full three-dimensional information in a set of one-dimensional plots. In principle it does not have to be an advantage, because full description of a correlation function requires infinite number of *l*, *m* components. But it so happens that the intrinsic symmetries of a pair distribution in a femtoscopic analysis result in most of the components to vanish. For the identical particles correlation functions, all coefficients with odd values of *l* and *m* disappear. It has also been shown, that the most significant portion of femtoscopic data is stored in the components with the lowest *l* values. It is expected that, the main femtoscopic information is contained in the following components [25]:

$$C_0^0 \to R_{LCMS}\ , \tag{3.22}$$

$$\Re C_2^0 \to \frac{R_T}{R_{long}}\ , \tag{3.23}$$

$$\Re C_2^2 \to \frac{R_{out}}{R_{side}}\ , \tag{3.24}$$

where $R_{LCMS} = \sqrt{\left({R_{out}}^2 + {R_{side}}^2 + {R_{long}}^2\right)/3}$ and $R_T = \sqrt{\left(R_{out}^2 + R_{side}^2\right)/2}$. The C_0^0 is sensitive to the overall size of a correlation function. The $\Re C_2^0$ carries the information about the ratio of the transverse to the longitudinal radii, due to its $\cos^2(\theta)$ weighting in Y_2^0. The component $\Re C_2^2$ with its $\cos^2(\phi)$ weighting encodes the ratio between outward and sideward radii. Thus, the spherical harmonics method allows to obtain and analyze full three-dimensional femtoscopic information from a correlation function [25].

3.3 Experimental approach

The correlation function is defined as a probability to observe two particles together divided by the product of probabilities to observe each of them separately (Eq. 3.16). Experimentally this is achieved by dividing two distributions of relative momentum of pairs of particles coming from the same event and the equivalent distribution of pairs where each particle is taken from different collisions. In this way, one obtains not only femtoscopic information but also all other event-wide correlations. This method is useful for experimentalists to estimate the magnitude of non-femtoscopic effects. There exists also a different approach, where two particles in pairs in the second distribution are also taken from the same event. The second method gives only information about physical effects accessible via femtoscopy. The aim of this work is a study of effects coming from two particle interferometry, hence the latter method was used.

In order to calculate experimental correlation function, one uses the following approach. One has to construct two histograms: the *numerator* N and the *denominator* D with the particle pairs momenta, where particles are coming from the same event. Those histograms can be one-dimensional (as a function of $|\mathbf{q}|$), three dimensional (a function of three components of $\mathbf{q}$ in LCMS) or a set of one-dimensional histogram representing components of the spherical harmonic decomposition of the distribution. The second histogram, D is filled for each pair with the weight 1.0 at a corresponding relative momentum $\mathbf{q} = 2\mathbf{k}^*$. The first one, N is filled with the same procedure, but the weight is calculated as $|\Psi_{ab}(\mathbf{r}^*, \mathbf{k}^*)|^2$. A division N/D gives the correlation function C. This procedure can be simply written as [25]:

$$C(\mathbf{k}^*) = \frac{N}{D} = \frac{\sum\limits_{n_i \in D} \delta(\mathbf{k^*}_i - \mathbf{k}^*) |\Psi_{ab}(\mathbf{r^*}_i, \mathbf{k^*}_i)|^2}{\sum\limits_{n_i \in D} \delta(\mathbf{k^*}_i - \mathbf{k}^*)} \ . \tag{3.25}$$

The D histogram represents the set of all particle pairs used in calculations. The n_i is a pair with the its relative momentum $\mathbf{k^*}_i$ and relative separation $\mathbf{r^*}_i$. The wave function used in Eq. 3.25 has one of the following forms:

$$|\Psi_{\pi\pi}(\mathbf{r}^*, \mathbf{k}^*)|^2 = |\Psi_{KK}(\mathbf{r}^*, \mathbf{k}^*)|^2 = 1 + \cos(2\mathbf{k}^*\mathbf{r}^*) \ , \tag{3.26}$$

$$|\Psi_{pp}(\mathbf{r}^*, \mathbf{k}^*)|^2 = 1 - \frac{1}{2}\cos(2\mathbf{k}^*\mathbf{r}^*) \ . \tag{3.27}$$

The first one is used in case of bosons, and the latter one is for identical fermions. Mathematically, the procedure of calculating the Eq. 3.25 is equivalent to a calculation of an integral in Eq. 3.17 through a Monte-Carlo method.

3.4 Scaling of femtoscopic radii

In the hydrodynamic models describing expansion of a quark-gluon plasma, particles are emitted from the source elements. Each of the source elements is moving with the velocity u_μ given by hydrodynamic equations. Because solutions of those equations are smooth, nearby source elements have similar velocities. Each emitted particle from a certain source element is boosted with the flow velocity u_μ according to the point of origin. Hence particles emitted close to each other (pairs with large transverse momentum $|\mathbf{k}_T|$) will gain the similar velocity boost, they can combine into pairs with small relative momenta ($|\mathbf{q}|$) and therefore become correlated. If the two particles are emitted far away from each other (a pair with small $|\mathbf{k}_T|$), the flow field u_μ in their point of emission might be very different and it will be impossible for them to have sufficiently small relative momenta in order to be in region of interference effect. This effect is visible in a width of a correlation function in the Fig. 3.4. The correlation function gets broader for greater values of $|\mathbf{k}_T|$ and the femtoscopic radius R becomes smaller [8, 27].

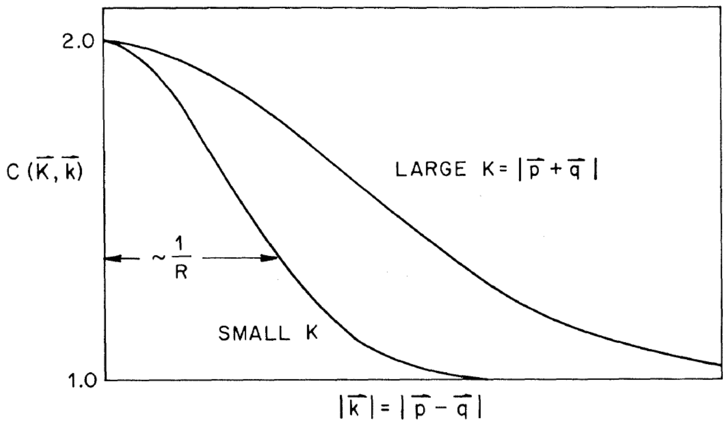

Figure 3.4: Correlation function width dependence on total pair momentum. Pion pairs with a large total momentum are more correlated [27].

3.4.1 Scaling in LCMS

Hydrodynamic calculations performed in LCMS show that femtoscopic radii in outward, sideward, and longitudinal direction show dependence on transverse mass $m_T = \sqrt{k_T^2 + m^2}$, where m is a mass of a particle [28]. Moreover, experimental results show that this scaling is observed for R_{LCMS} radii also. This dependence can be expressed as follows:

$$\boxed{R_i = \alpha m_T^{-\beta}} \tag{3.28}$$

where i subscript indicates that this equation applies to R_{out}, R_{side} and R_{long} radii. The β exponent is approximately equal 0.5. In case of strong transversal expansion of the emitting source, the decrease of longitudinal interferometry radius can be more quick than $m_T^{-0.5}$, hence one can expect for longitudinal radii greater values of $\beta > 0.5$ [28].

3.4.2 Scaling in PRF

In the collisions at the LHC energies, pions are most abundant particles and their multiplicities are large enough to enable three-dimensional analysis. However, for heavier particles, such as kaons and protons statistical limitations arise. Hence it is often possible to only measure one-dimensional radius R_{inv} for those particles. The R_{inv} is then calculated in the PRF. The transition from LCMS to PRF is a Lorentz boost in the direction of pair transverse momentum with velocity $\beta_T = p_T/m_T$. Hence only R_{out} radius changes:

$$R^*_{out} = \gamma_T R_{out} \ . \tag{3.29}$$

The one-dimensional R_{inv} radius is direction-averaged source size in PRF. One can notice, that such power-law scaling of R_{inv} described by Eq. 3.28 is not observed. To recover such scaling in PRF one has to take into consideration two effects when transforming variables from LCMS to PRF: overall radius growths and source distribution becomes non-Gaussian, while developing long-range tails (see Fig. 3.3 for an example). The interplay of these two effects can be accounted with an approximate formula:

$$R_{inv} = \sqrt{\left({R_{out}}^2\sqrt{\gamma_T} + {R_{side}}^2 + {R_{long}}^2\right)/3}\ . \tag{3.30}$$

Assuming that all radii are equal $R_{out} = R_{side} = R_{long}$ this formula can be simplified:

$$\boxed{R_{LCMS} \approx R_{inv} \times [(\sqrt{\gamma_T} + 2)/3]^{-1/2}}\ . \tag{3.31}$$

This approximate formula allows to restore power-law behaviour of the scaled radii not only when the radii are equal, but also when their differences are small (for explanation see the last part of the section 3.2.3).

This method of recovering scaling in PRF can be used as a tool for the search of hydrodynamic collectivity between pions, kaons and protons in heavy ion collisions with the measurement of one-dimensional radius in PRF.

Chapter 4

Results

For the purposes of the femtoscopic analysis in this thesis, the THERMINATOR model was used to generate large number of events for eight different sets of initial conditions corresponding the following centrality ranges: 0-5%, 0-10%, 10-20%, 20-30%, 30-40%, 40-50%, 50-60% and 60-70% for the Pb-Pb collisions at the centre of mass energy $\sqrt{s_{NN}} = 2.76$ TeV.

4.1 Identical particles correlations

The correlation functions (three-dimensional and one-dimensional) were calculated separately for the following different pairs of identical particles: π-π, K-K and p-p for nine k_T bins (in GeV/c): 0.1-0.2, 0.2-0.3, 0.3-0.4, 0.4-0.5, 0.6-0.7, 0.7-0.8, 0.8-1.0 and 1.0-1.2. In case of kaons, k_T ranges start from 0.3 and for pions from 0.4 and for both of them the maximum value is 1.0. The k_T ranges for the heavier particles were limited to maintain sufficient multiplicity to perform reliable calculations.

4.1.1 Spherical harmonics components

The three-dimensional correlation function as a function of relative momentum q_{LCMS} was calculated in a form of components of spherical harmonics series accordingly to the Eq. 3.21. In the femtoscopic analysis of identical particles, the most important information is stored in the $\Re C_0^0$, $\Re C_2^0$ and $\Re C_2^2$, hence only those components were analyzed. Correlation functions obtained in this procedure were calculated for the different centrality bins for the pairs of pions, kaons and protons. They are presented in the Fig. 4.1, 4.2 and 4.3.

Coefficients for pairs of identical bosons (pions and kaons) are shown in the Fig. 4.1 and 4.2. The wave function symmetrization (Bose-Einstein statistics) causes the increase of a correlation in the low relative momenta regime ($q_{LCMS} < 0.06$ GeV/c or even $q_{LCMS} < 0.12$ GeV/c for more peripheral collisions). It is clearly visible in the $\Re C_0^0$ component. The $\Re C_0^0$ resembles one-dimensional correlation function and in fact it encodes information about overall source radius. The second coefficient $\Re C_2^0$ differs from zero (is negative), which yields the information about the ratio R_T/R_{long}. The $\Re C_2^2$ stores the R_{out}/R_{side} ratio and one can notice that is non-vanishing (is also negative).

The correlation function for a pair of identical fermions is presented in the Fig. 4.3. An influence of wave function anti-symmetrization (Fermi-Dirac statistics) has its effect in the decrease of a correlation down to 0.5 at low relative momentum ($q_{LCMS} < 0.1$ GeV/c or $q_{LCMS} < 0.15$ GeV/c for more peripheral collisions), which can be observed in $\Re C_0^0$. The $\Re C_2^0$ and $\Re C_2^2$ coefficients differ from zero and are becoming positive.

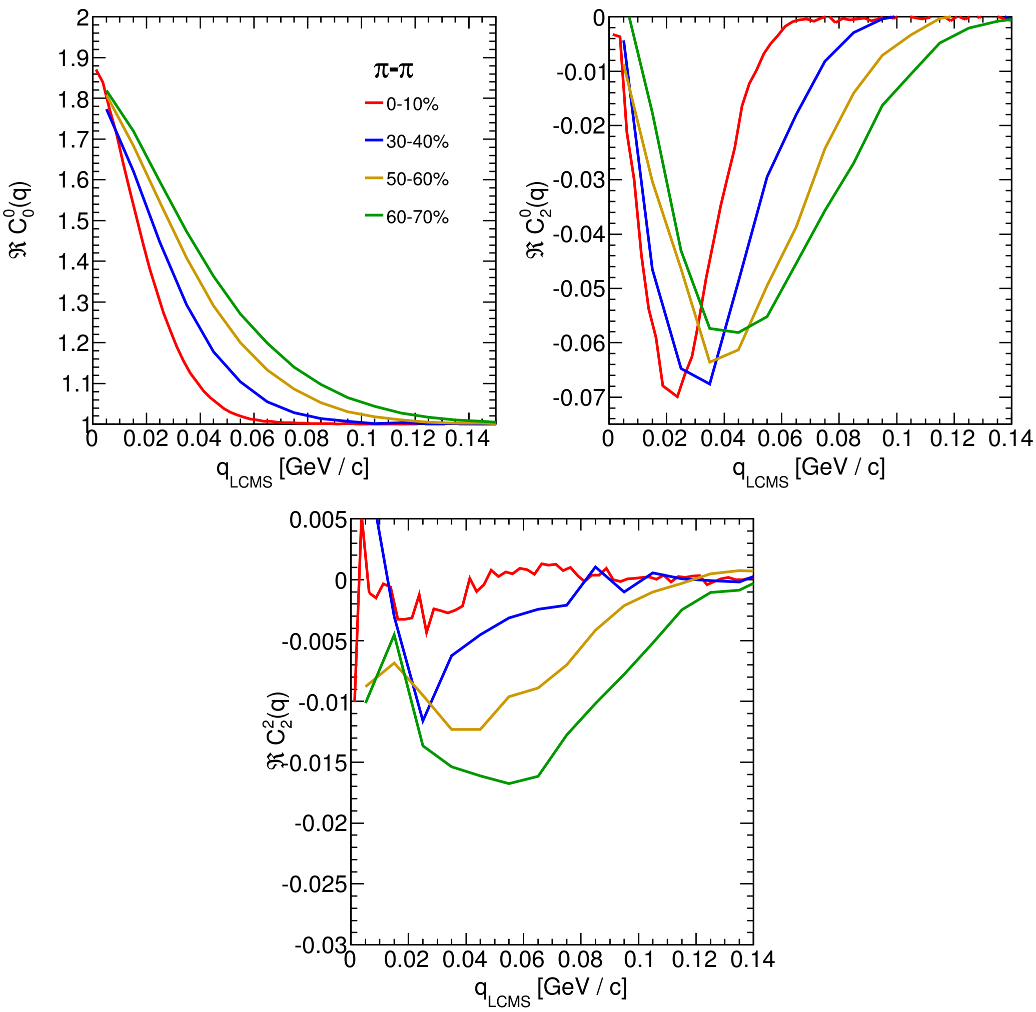

Figure 4.1: Spherical harmonics coefficients of the two-pion correlation function. From the top left: $\Re C_0^0$, $\Re C_2^0$ and $\Re C_2^2$. Only few centrality bins are presented for increased readability.

The common effect of the spherical harmonics form of a correlation function is the "mirroring" of the shape of the $\Re C_0^0$ coefficient - when correlation function increases at low q_{LCMS}, the $\Re C_2^0$ and $\Re C_2^2$ are becoming negative and vice versa. This is quite different behaviour than in the case of correlations of non-identical particles, where the $\Re C_0^0$ still behaves in the same manner, but $\Re C_2^2$ has the opposite sign to the $\Re C_2^0$ [25].

In all cases, the correlation function gets wider with the peripherality of a collision i.e. the correlation function for most central collisions (0-10%) is much narrower than for the most peripheral ones (60-70%). This phenomena in clearly

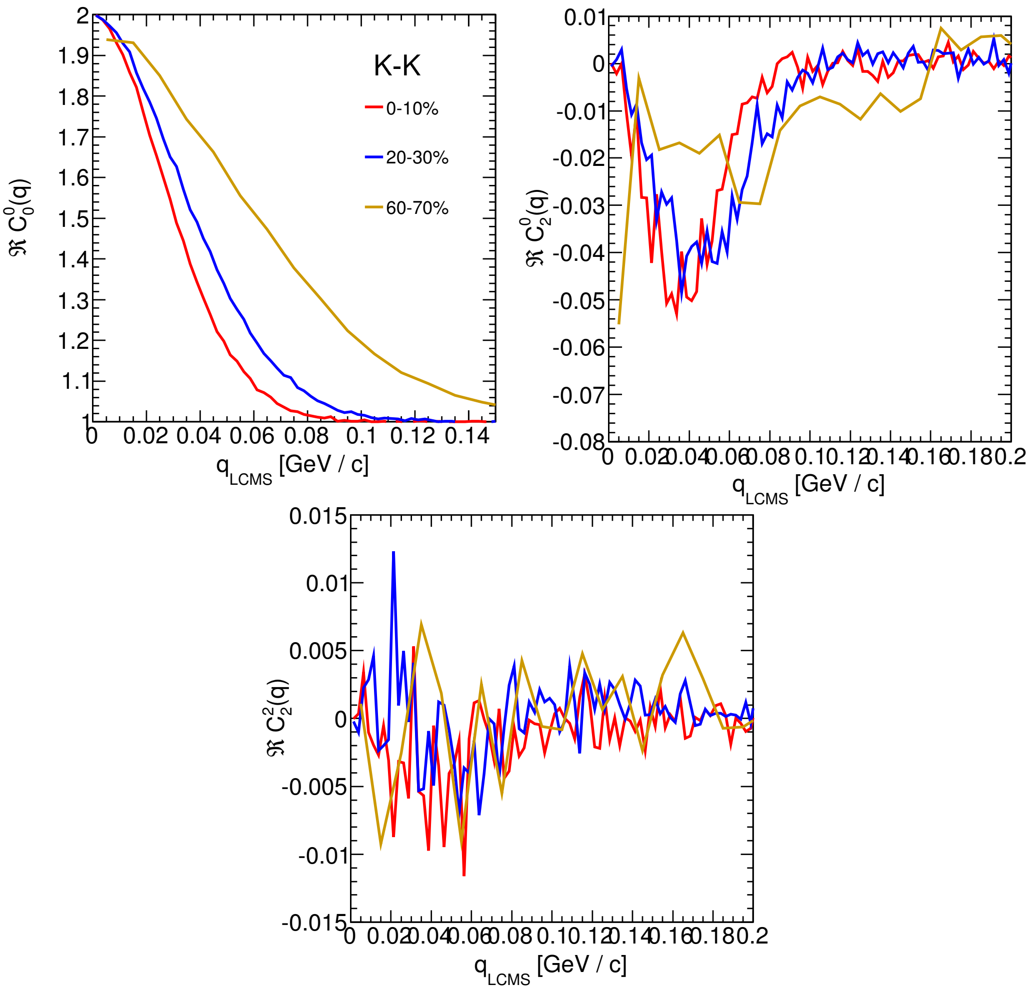

Figure 4.2: Spherical harmonics coefficients of the two-kaon correlation function. From the top left: $\Re C_0^0$, $\Re C_2^0$ and $\Re C_2^2$. Only few centrality bins are presented for increased readability. The $\Re C_2^2$ is noisy, but one can still notice that it differs from zero and is becoming negative.

visible the $\Re C_0^0$ coefficients. Other components are also affected by this effect, this is especially noticeable in the case of kaons and pions. For the protons, the results are noisy, hence this effect is not clearly distinguishable.

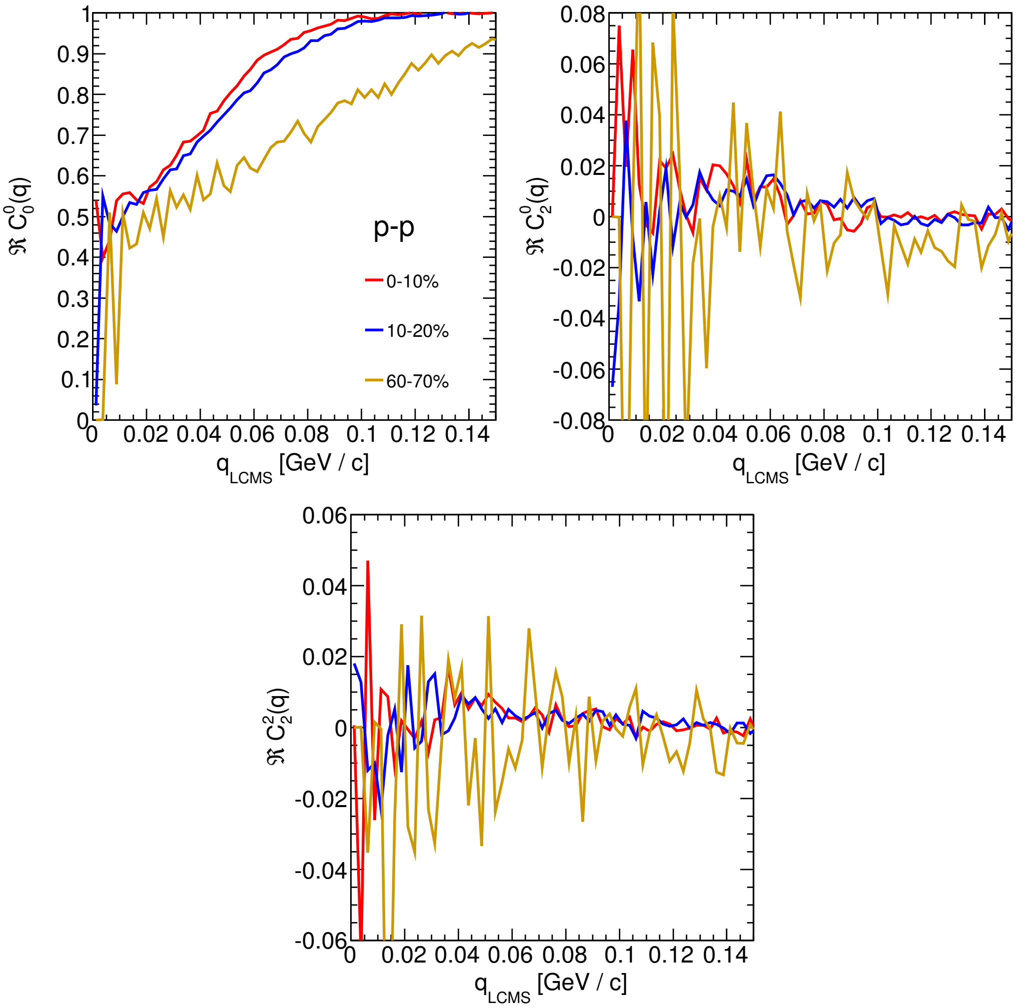

Figure 4.3: Spherical harmonics coefficients of the two-proton correlation function. From the top left: $\Re C_0^0$, $\Re C_2^0$ and $\Re C_2^2$. Only few centrality bins are presented for increased readability. The $\Re C_2^0$ and $\Re C_2^2$ are noisy, but one can still notice, that they differ from zero and are becoming positive.

4.1.2 Centrality dependence of a correlation function

The centrality dependence of a correlation function is especially visible in one-dimensional correlation functions. This effect is presented in the Fig. 4.4 - the correlation functions for pions, kaons and protons are plotted for the same k_T range but different centrality bins. One can notice that the width of a function is smaller in the case of most central collisions. Hence, the femtoscopic radii (proportional to the inverse of width) are increasing with the centrality. An explanation for this growth is that in the most central collisions, a size of a created system is larger than for the peripheral ones.

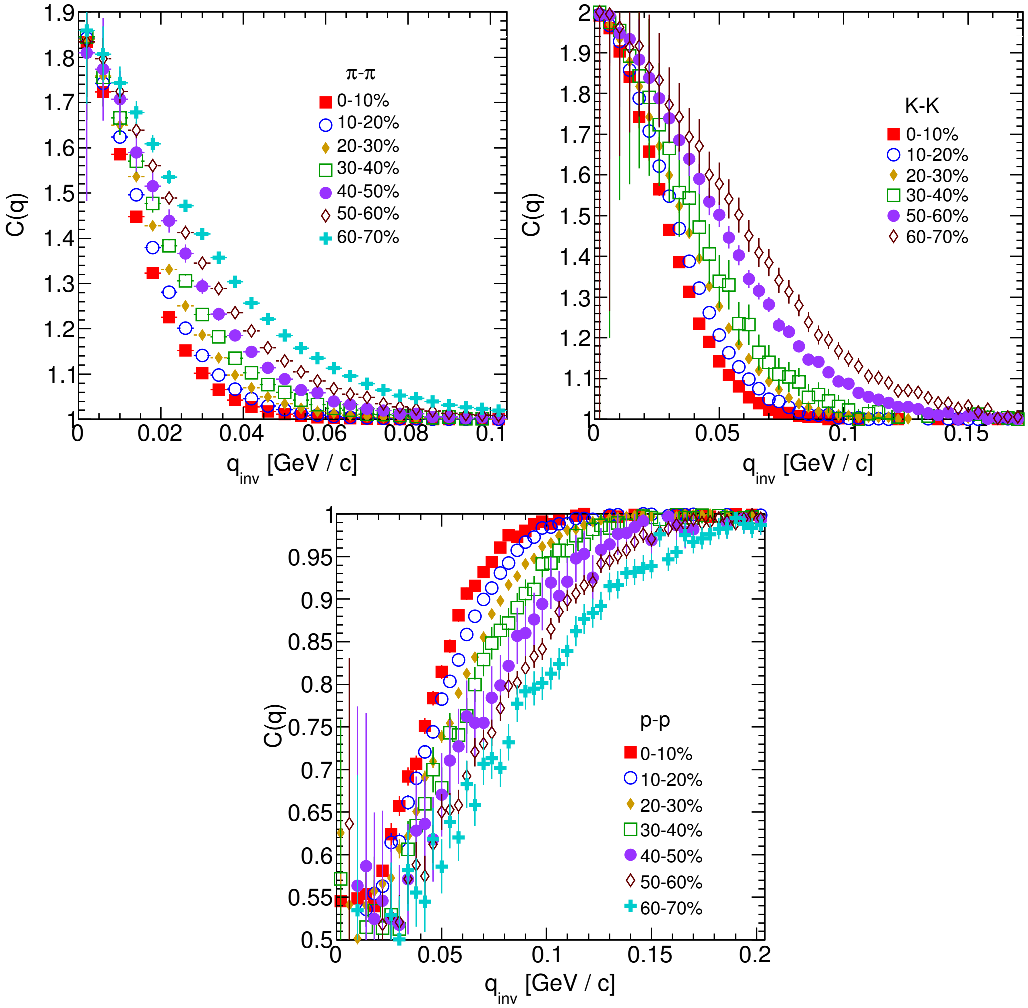

Figure 4.4: One-dimensional correlation function for pions(top left), kaons (top right) and protons (bottom) for different centralities.

4.1.3 k_T dependence of a correlation function

In the Fig. 4.5 there are presented one-dimensional correlation functions for pions, kaons and protons for the same centrality bin, but different k_T ranges. One can observe in all cases of the particle types, appearance of the same trend: with the increase of the total transverse momentum of a pair, the width of a correlation function increases and the femtoscopic radius decreases. The plots in the Fig. 4.5 were zoomed in to show the influence of k_T.

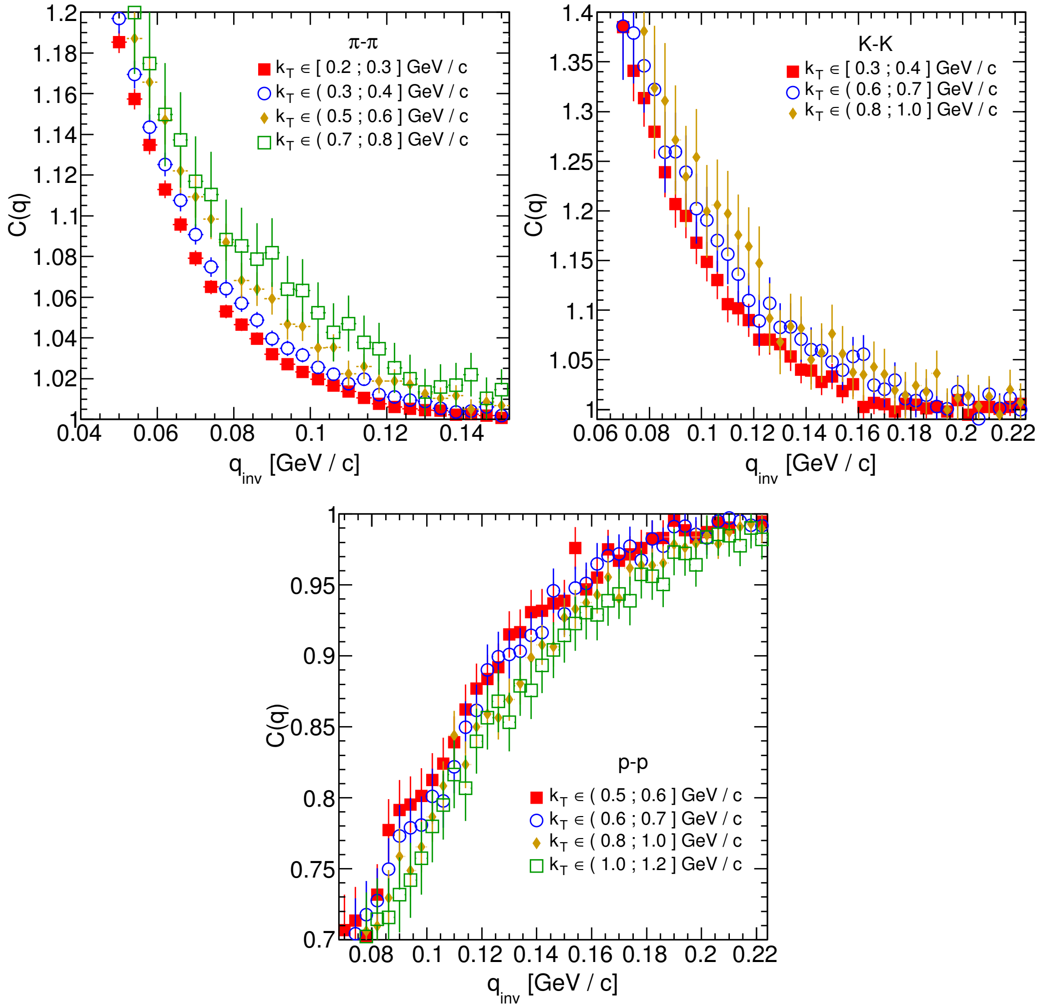

Figure 4.5: One-dimensional correlation functions for pions, kaons and protons, for the same centrality bin and different k_T ranges. The plot was zoomed in to the region which illustrates the k_T dependence in the best way. Only few of the calculated ranges are presented for better readability.

4.2 Results of the fitting procedure

In order to perform a quantitative analysis of a wide range of correlation functions, the theoretical formulas were fitted to the calculated experimental-like data. In this procedure, the femtoscopic radii for the three-dimensional as well as one-dimensional correlation functions were extracted. The main goal of this analysis is a verification of a common transverse mass scaling for different particles types. Obtained radii are plotted as a function of a transverse mass $m_T = \sqrt{k_T^2 + m^2}$. To test the scaling, the following power-law was fitted to the particular radii afterwards:

$$R_x = \alpha {m_T}^{-\beta} \,, \tag{4.1}$$

where the α and β are free parameters.

4.2.1 The three-dimensional femtoscopic radii scaling

In the Fig. 4.6 there are presented femtoscopic radii in the outward, sideward and longitudinal directions for the analysis of two-pion correlation functions in

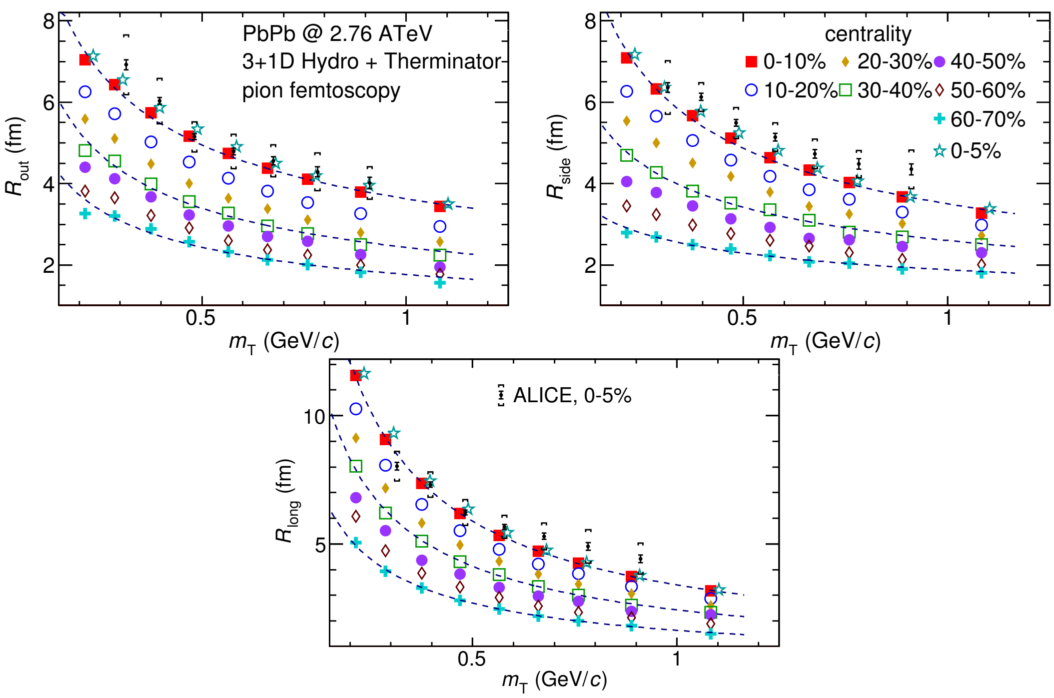

Figure 4.6: Femtoscopic radii in LCMS coming from two-pion correlation functions for all centrality bins as a function of m_T. The dashed lines are power-law fits. The most central collisions (0-5%) are compared to the results from ALICE [29]. The two datasets are shifted to the right for visibility [30].

the LCMS. The dashed lines are fits of the power law to the data. One can notice, that the power law describes well data points with a 5% accuracy. The β fit parameter for the outward direction is in the order of 0.45. For the sideward direction, this parameter has the similar value, but it is lower for the most peripheral collisions. In case of the longitudinal direction, the β has greater value, up to 0.75. In the Fig. 4.6 there are also compared results for the top 5% central collisions (star-shaped markers) with experimental data from ALICE [29]. The experimental results are consistent with the ones coming from the model predictions.

The Fig. 4.7 presents femtoscopic radii coming from the kaon calculations. The R_{out}, R_{side} and R_{long} fall also with the power-law within the 5% accuracy. The β parameter was larger in case of kaons: 0.59 in outward direction, 0.54 in the sideward and 0.86 for longitudinal.

The results for two-proton analysis are shown in the Fig. 4.8. The Eq. 4.1 was fitted to the data and tells that the protons also follow the m_T scaling within 5% range. The β parameter values were even bigger for the outward (0.58), sideward (0.61) and longitudinal (1.09) directions than for the other particle types.

The Fig. 4.9 presents results for the pions, kaons and protons together as a function of m_T. Considering differences in the β value for the fits for differ-

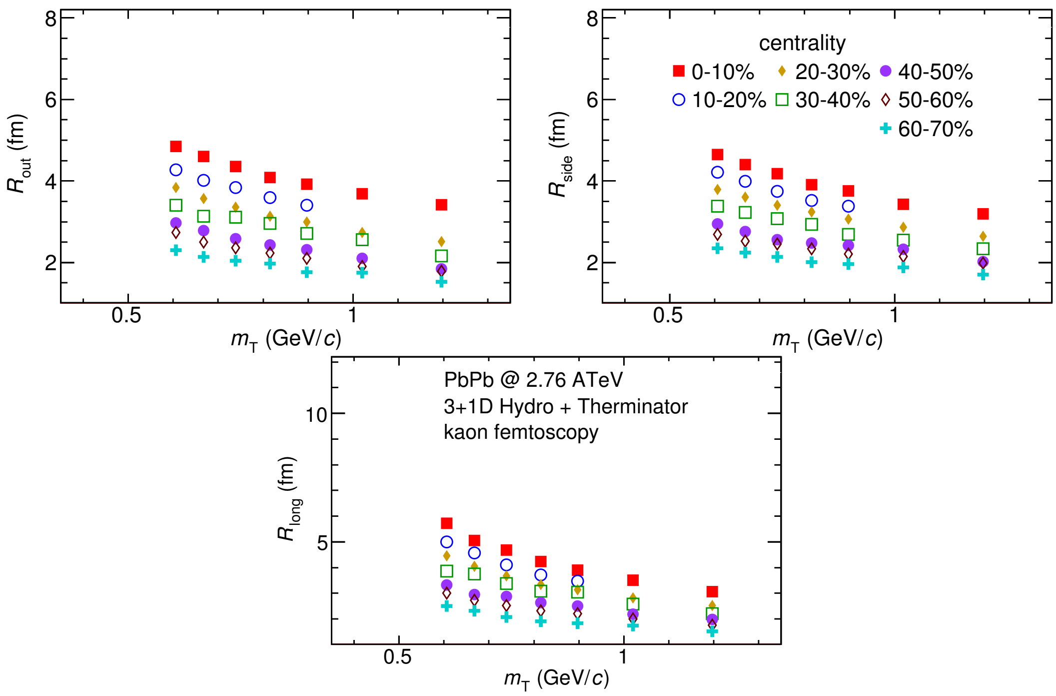

Figure 4.7: Femtoscopic radii extracted from two-kaon correlation functions for different centrality bins as a function of m_T. [30].

ent particles, one can suspect that there is no common scaling between different kinds of particles. However, when all of the results shown on the same plot, they are aligning on the common curve and the scaling is well preserved. The scaling accuracy is 3%, 5% and 4% for the 0-10%, 20-30% and 60-70% for the outward direction. For the sideward radii the scaling is better, with average deviations 2%, 2% and 3% respectively. In case of longitudinal direction the accuracy is 6%, 5% and 3% for the three centralities. The β parameter for the outward direction is close to the 0.42 in all cases. For the sideward direction it varies from 0.28 to 0.47 and is bigger for more central collisions. Regarding longitudinal radii, the exponent is bigger than the other two: $\beta \in [0.62; 0.72]$. Considering all results, the plotted radii are following the common power-law scaling within the 5% accuracy for all directions, centralities and particle types.

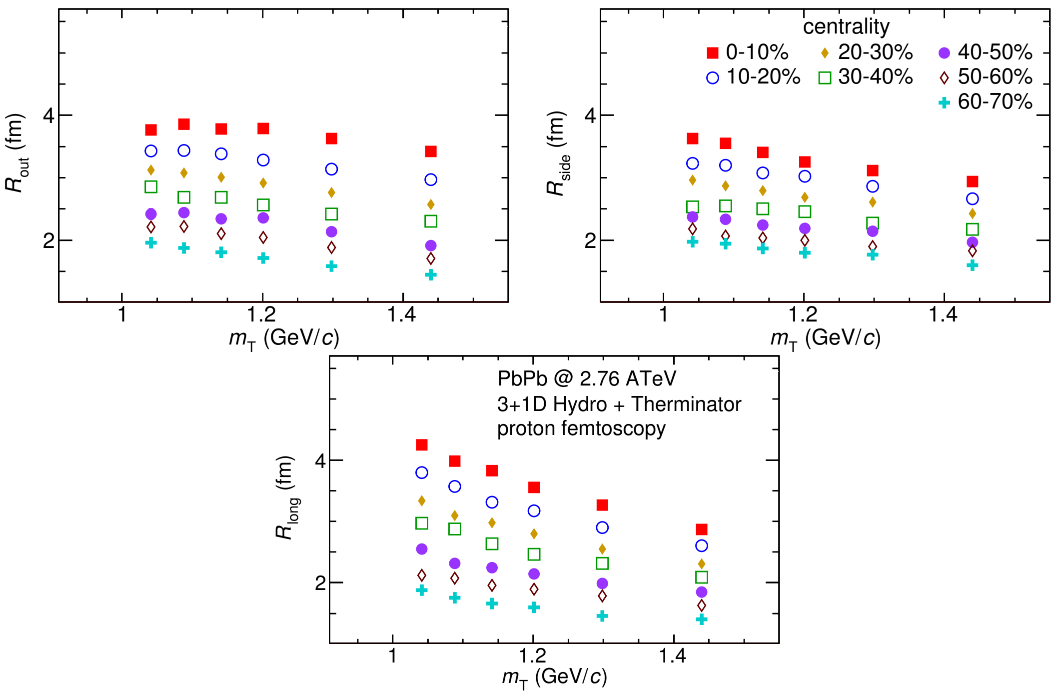

Figure 4.8: Femtoscopic radii extracted from two-proton correlation functions for different centrality bins as a function of m_T. [30].

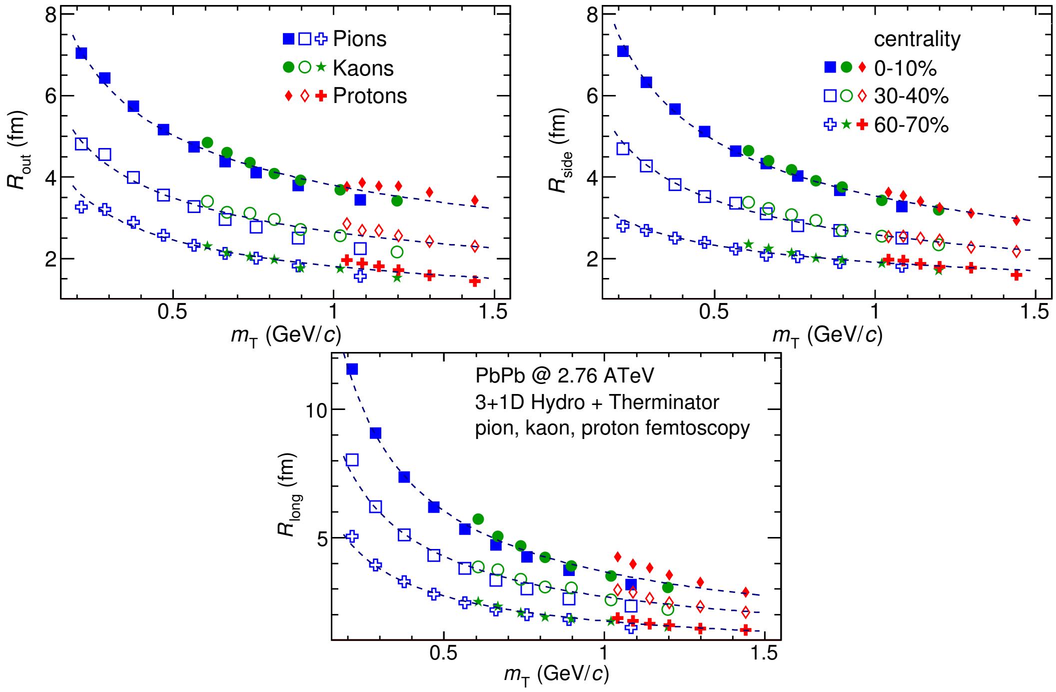

Figure 4.9: The results from the calculations for the pions, kaons and protons in for the three centralities presented on the common plot. One can notice that radii for particular centralities and different particle types follow the common power-law scaling. [30].

4.2.2 Scaling of one-dimensional radii

To the one-dimensional correlation function, the corresponding function in the PRF given by the Eq. 3.18 was fitted. The results from those fits are presented in the upper left plot in the Fig. 4.10. One immediately notices, that there is no common scaling of R_{inv} for different kind of particles. In the Fig. 4.9 the radii in the outward direction for the pions, kaons and protons for the same m_T are similar. However, when one performs a transition from the LCMS to the PRF, the R_{out} radius grows:

$$R_{out}{}^{*} = \gamma_T R_{out} \,, \tag{4.2}$$

where $\gamma_T = m_T/m$. For the lighter particles, the γ_T is much larger, hence the bigger growth of the R_{out} and the overall radius. This is visible in the Fig. 4.10 (top left), where the radii in the PRF for the lighter particles are bigger than for the heavier ones in case of the same m_T range.

In the Fig. 4.9 there is visible scaling in the outward, sideward and longitudinal direction. Hence one can expect an appearance of such scaling in a direction-averaged radius calculated in the LCMS. This radius is presented in the Fig. 4.10 (bottom) and indeed the R_{LCMS} exhibits power-law scaling with the m_T.

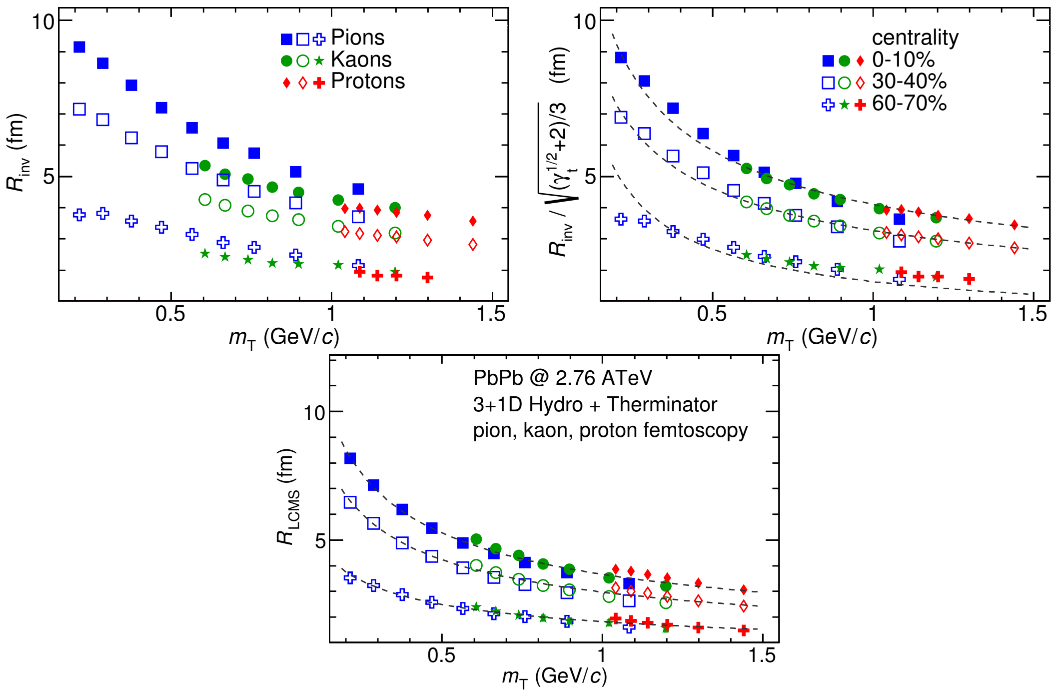

Figure 4.10: Top left: one-dimensional radius for pions, kaons and protons calculated in the PRF. Top right: the R_{inv} scaled by the proposed factor. Bottom: averaged one-dimensional radius in the LCMS for pions, kaons and protons. Only three centrality bins are shown for the better readability [30].

One can try to account the effect of an increase of the radii in the outward direction by using the appropriate scaling factor. In the Fig. 4.10 (top right) there are femtoscopic radii in the LCMS divided by the proposed scaling factor:

$$f = \sqrt{(\sqrt{\gamma_T} + 2)/3}\ . \tag{4.3}$$

The radii for pions, kaons and protons in the PRF after the division by f are following the power-law with the accuracy of 10%.

4.3 Discussion of the results

The femtoscopic radii obtained from the three-dimensional correlation function fitting exhibit the m_T dependence described by the power law (Eq. 4.1). This scaling is preserved quite well with accuracy <10%. Observation of such scaling in a femtoscopic radii is a strong signal of appearance of a collective behaviour of a particle-emitting source created in the collision. The data used in the analysis was coming from the hydrodynamic model, hence one can indeed expect the appearance of this scaling. However, the results for pion femtoscopy from the ALICE at LHC are consistent with the data from analysis performed in this thesis (Fig. 4.6). This is a confirmation of an applicability of hydrodynamic models in a description of an evolution of a quark-gluon plasma.

The β parameter calculated in the fitting of the power-law to the femtoscopic radii is in the order of 0.5 in case of the radii in the transverse plane. This value is consistent with the hydrodynamic predictions. In case of longitudinal radii, the exponent is bigger (greater than 0.7), which is an indication of a strong transversal expansion in the system [28].

A scaling described above is visible in the LCMS, however due to limited statistics, analysis in this reference frame is not always possible. In such case one performs calculations in the PRF. The m_T scaling in the PRF is not observed - this has the trivial kinematic origin. A transition from the PRF to LCMS causes growth of the radius in the outward direction and the common power-law scaling for different particles breaks due to differences in the $\gamma_T(m_T)$ for different particle types. However one can try to deal with the radius growth and restore the scaling by multiplying the radii R_{inv} by an approximate factor $\sqrt{\left(\sqrt{\gamma_T}+2\right)/3}$. The scaled R_{inv} are following the power-law and could be used as a verification of hydrodynamic behaviour in the investigated particle source.

The hadronic evolution and freeze-out in the `THERMINATOR` is followed by the resonance propagation and decay phase. A good accuracy of a scaling with the power-law indicated that the inclusion of the resonances does not break the m_T scaling. However, recent calculations including also hadron rescattering phase indicate that the scaling between pions and kaons is broken at the LHC [31].

Conclusions

This thesis presents the results of the two-particle femtoscopy of different particle kinds produced in Pb-Pb collisions at the centre of mass energy $\sqrt{s_{NN}} = 2.76$ TeV. The analysed data was generated by the THERMINATOR model using the (3+1)-dimensional hydrodynamic model.

The momentum correlations were studied for three different types of particle pairs: pions, kaons and protons. The data was analyzed for eight different sets of initial conditions corresponding the following centrality ranges: 0-5%, 0-10%, 10-20%, 20-30%, 30-40%, 40-50%, 50-60% and 60-70%. The correlation functions were calculated for the nine k_T bins from 0.1 Gev/c to 1.2 GeV/c. The calculations were performed using spherical harmonics decomposition of a three-dimensional correlation function. Using this approach, one can obtain full three-dimensional information about the source size using only the three coefficients: $\Re C_0^0$, $\Re C_2^0$ and $\Re C_2^2$. To perform further quantitative analysis, the femtoscopic radii were extracted through fitting.

The calculated correlation functions show expected increase of a correlation at low relative momenta in case of identical bosons (pions and kaons) and the decrease for the identical fermions (protons) respectively. This effect is especially visible in the first spherical harmonic coefficient $\Re C_0^0$. The other two components $\Re C_2^0$ and $\Re C_2^2$ are non-vanishing and are providing information about the ratios of radii in the outward, sideward and longitudinal directions.

An increase of width of a correlation function with the peripherality of a collision and the k_T is observed for pions, kaons and protons. This increase of femtoscopic radii (proportional to the inverse of width) with the k_T is related with the m_T scaling predicted by the hydrodynamic calculations.

Hydrodynamic equations are predicting appearance of femtoscopic radii common scaling for different kinds of particles with the $m_T^{-0.5}$ in the LCMS. In the results in this work, a common scaling for different particle types is observed in the LCMS in the outward, sideward and longitudinal direction. The direction-averaged radius R_{LCMS} also shows this power-law behaviour. The fitting of a power law $\alpha m_T^{-\beta}$ to the femtoscopic radii yielded the information, that the β exponent for the outward and sideward direction is in order of 0.5, which is consistent with the hydrodynamic predictions. For the longitudinal direction, the β is bigger (>0.7) than in the other directions which is an indication of a strong transverse flow. Femtoscopic radii in LCMS are following the power-law scaling with the accuracy <5% for pions and kaons, and <10% in case of protons.

In case of the one-dimensional radii R_{inv} calculated in the PRF, no common scaling is observed. This is a consequence of a transition from the LCMS to the PRF, which causes the growth of radius in the outward direction and breaks the scaling for different particles. However, one can try to correct the influence of the R_{out} growth with an approximate factor $\sqrt{\left(\sqrt{\gamma_T}+2\right)/3}$. After the division of the R_{inv} by the proposed factor, the scaling is restored with an accuracy <10%. In this way, the experimentally simpler measure of the one-dimensional radii can be used as a probe for the hydrodynamic collectivity.

The THERMINATOR model includes hydrodynamic expansion, statistical hadronization, resonance propagation and decay afterwards. The m_T scaling is predicted from the pure hydrodynamic calculations. However, this study shows, that influence of the resonances on this scaling is less than 10%.

Appendix A

asdf

Appendix A

asdf

Appendix A

asdf

Bibliography

[1] Standard Model of Elementary Paticles - Wikipedia, the free encyclopedia `http://en.wikipedia.org/wiki/standard_model`.

[2] R. Aaij et al. (LHCb Collaboration). Observation of the resonant character of the $z(4430)^{-}$ state. *Phys. Rev. Lett.*, 112:222002, Jun 2014.

[3] Donald H. Perkins. *Introduction to High Energy Physics*. Cambridge University Press, fourth edition, 2000. Cambridge Books Online.

[4] G. Odyniec. *Phase Diagram of Quantum Chromo-Dynamics* - course at Faculty of Physics, Warsaw University of Technology, Jun 2012.

[5] J. Beringer et al. (Particle Data Group). The Review of Particle Physics. *Phys. Rev.*, D86:010001, 2012.

[6] Z. Fodor and S.D. Katz. The Phase diagram of quantum chromodynamics. 2009.

[7] F. Karsch. Lattice results on QCD thermodynamics. *Nuclear Physics A*, 698(1-4):199 – 208, 2002.

[8] Adam Kisiel. *Studies of non-identical meson-meson correlations at low relative velocities in relativistic heavy-ion collisions registered in the STAR experiment*. PhD thesis, Warsaw University of Technology, Aug 2004.

[9] J. Bartke. *Relativistic Heavy Ion Physics*. World Scientific Pub., 2009.

[10] W. Florkowski. *Phenomenology of Ultra-Relativistic Heavy-Ion Collisions*. World Scientific, 2010.

[11] Science Grid This Week, October 25, 2006 - Probing the Perfect Liquid with the STAR Grid `http://www.interactions.org/sgtw/2006/1025/star_grid_more.html`.

[12] K. Grebieszkow. Fizyka zderzeń ciężkich jonów, `http://www.if.pw.edu.pl/~kperl/hip/hip.html`.

[13] Ulrich W. Heinz. From SPS to RHIC: Maurice and the CERN heavy-ion programme. *Phys.Scripta*, 78:028005, 2008.

[14] J. Adams et al. Identified particle distributions in pp and Au+Au collisions at s(NN)**(1/2) = 200 GeV. *Phys.Rev.Lett.*, 92:112301, 2004.

[15] G. David, R. Rapp, and Z. Xu. Electromagnetic Probes at RHIC-II. *Phys.Rept.*, 462:176–217, 2008.

[16] A. Marin et al. Dilepton measurements with CERES. *PoS*, CPOD07:034, 2007.

[17] J. Adams et al. Experimental and theoretical challenges in the search for the quark gluon plasma: The STAR Collaboration's critical assessment of the evidence from RHIC collisions. *Nucl.Phys.*, A757:102–183, 2005.

[18] Adam Kisiel, Tomasz Taluc, Wojciech Broniowski, and Wojciech Florkowski. THERMINATOR: THERMal heavy-IoN generATOR. *Comput.Phys.Commun.*, 174:669–687, 2006.

[19] Mikolaj Chojnacki, Adam Kisiel, Wojciech Florkowski, and Wojciech Broniowski. THERMINATOR 2: THERMal heavy IoN generATOR 2. *Comput.Phys.Commun.*, 183:746–773, 2012.

[20] I. et al (BRAHMS Collaboration) Bearden. Charged meson rapidity distributions in central $\mathrm{Au}+\mathrm{Au}$ collisions at $\sqrt{s_{NN}} = 200\ \mathrm{GeV}$. *Phys. Rev. Lett.*, 94:162301, Apr 2005.

[21] W. Israel and J.M. Stewart. Transient relativistic thermodynamics and kinetic theory. *Annals of Physics*, 118(2):341 – 372, 1979.

[22] Piotr Bożek. Flow and interferometry in (3 + 1)-dimensional viscous hydrodynamics. *Phys. Rev. C*, 85:034901, Mar 2012.

[23] K. Kovtun, P. D. T. Son, and A. O. Starinets. Viscosity in strongly interacting quantum field theories from black hole physics. *Phys. Rev. Lett.*, 94:111601, Mar 2005.

[24] Fred Cooper and Graham Frye. Single-particle distribution in the hydrodynamic and statistical thermodynamic models of multiparticle production. *Phys. Rev. D*, 10:186–189, Jul 1974.

[25] Adam Kisiel. Nonidentical-particle femtoscopy at $\sqrt{s_{NN}} = 200$ GeV in hydrodynamics with statistical hadronization. *Phys. Rev. C*, 81:064906, Jun 2010.

[26] Adam Kisiel and David A. Brown. Efficient and robust calculation of femtoscopic correlation functions in spherical harmonics directly from the raw pairs measured in heavy-ion collisions. *Phys.Rev.*, C80:064911, 2009.

[27] S. Pratt. Pion Interferometry for Exploding Sources. *Phys.Rev.Lett.*, 53:1219–1221, 1984.

[28] S.V. Akkelin and Yu.M. Sinyukov. The HBT-interferometry of expanding inhomogeneous sources. *Z.Phys.*, C72:501–507, 1996.

[29] K. Aamodt et al. Two-pion Bose-Einstein correlations in central Pb-Pb collisions at $sqrt(s_N N)$ = 2.76 TeV. *Phys.Lett.*, B696:328–337, 2011.

[30] A. Kisiel, M. Galazyn, and P. Bozek. Pion, kaon, and proton femtoscopy in Pb–Pb collisions at $\sqrt{s_{\mathrm{NN}}}$=2.76 TeV modeled in 3+1D hydrodynamics. 2014.

[31] V.M. Shapoval, P. Braun-Munzinger, Iu.A. Karpenko, and Yu.M. Sinyukov. Femtoscopy correlations of kaons in $Pb + Pb$ collisions at LHC within hydrokinetic model. 2014.

List of Figures